INVESTIGATION OF POINT DEFECTS IN LITHIUM NIOBATE BY ELECTRON SPIN RESONANCE, ELECTRON NUCLEAR DOUBLE RESONANCE, AND OPTICAL ABSORPTION

By

MOHAMMAD REZA HANTEHZADEH

Bachelor of Science in Electrical Engineering
Oklahoma State University
Stillwater, Oklahoma
1981

Master of Science
Oklahoma State University
Stillwater, Oklahoma
1984

Submitted to the Faculty of the
Graduate College of the
Oklahoma State University
in the partial fulfillment of
the requirements for
the degree of
DOCTOR OF PHILOSOPHY
December, 1987

INVESTIGATION OF POINT DEFECTS IN LITHIUM NIOBATE BY ELECTRON SPIN RESONANCE, ELECTRON NUCLEAR DOUBLE RESONANCE, AND OPTICAL ABSORPTION

Thesis Approved:

Larry E. Halliburton
Thesis Advisor

Dean of the Graduate college

ACKNOWLEDGEMENTS

I would like to thank my major advisor, Dr. L. E. Halliburton, for his patience, guidance and help, without which the completion of this dissertation would have been impossible. Gratitude is also expressed to professors R. C. Powell, S. W. S. McKeever, and Z. Al-Shaieb who served on my committee. I would like to thank the people in the lab who created a friendly atmosphere during the course of this investigation. Special thanks to Dr. Michael Mombourquette for the help and support provided during the last phase of this dissertation. Financial support provided by the Radiation Safety Program at Oklahoma State University and the Air Force Office of Scientific Research is greatly appreciated. Finally I would like to thank my wife for her help, sacrifices, and steadfast support during the completion of this dissertation, and also my parents for their support and patience during my graduate studies.

TABLE OF CONTENTS

LIST OF FIGURES

CHAPTER I

INTRODUCTION

Lithium niobate ($LiNbO_3$) is a ferroelectric crystal with a high Curie temperature ($T_C \simeq 1200^oC$). This material is widely used in integrated optic switches and modulators, parametric oscillators, optical frequency doublers, etc. Its unique combination of properties such as large electro-optic coefficients, strong piezoelectric coefficients, excellent acoustic properties, and large birefringence means that $LiNbO_3$ offers highly efficient interactions between optic, acoustic, and electric fields in a single medium.

Crystal Growth

Lithium niobate is a dielectric material that does not exist in nature, but can easily be grown in the laboratory. It was described for the first time in 1928 by Zachariasen [1]. Matthias and Remeika [2] in 1949 studied single crystals grown from a flux and discovered the ferroelectric properties of $LiNbO_3$. However, the widespread use of this material did not begin until 1965 when Ballman [3] reported the successful growth of single crystals of $LiNbO_3$ by the Czochralski technique.

Simultaneously with Ballman's work, Fedulov, Shapiro

and Ladyzhenskii [4] also successfully used the Czochralski technique to grow $LiNbO_3$ crystals. A series of detailed characterization studies of the special properties of this unique material began with growth of single-domain crystals by Nassau and coworkers [5,6,7] in 1966.

Stoichiometry

Detailed characterization of the physical properties of $LiNbO_3$ is made more difficult by its complex solid state chemistry. Early optical and dielectric studies of $LiNbO_3$ by Fay, Alford, and Dess [8] in 1968 and Bergman, Ashkin, Ballman, Dziedzic, Levinstein, and Smith [9] in 1968 indicated that the properties of these crystals, such as Curie temperature and optical birefringence, depend on the melt composition from which they are grown. Subsequent crystal growth and x-ray diffraction studies of the phase diagram of the Li_2O-Nb_2O_5 system by Lerner, Legras, and Dumas [10] showed that this dependence results from the existence of solid solutions which incorporate both excess Li_2O and Nb_2O_5. They established that the congruent melting point of $LiNbO_3$ occurs at 48.6 mole percent Li_2O.

Thus, crystals pulled from a stoichiometric melt, i.e., lithium to niobium ratio of 1, will deviate significantly from stoichiometry and their composition will be inhomogeneous along the growth direction. Confirmation of these results by Carruthers, Peterson, Grasso, and Bridenbaugh [11] in 1971 led to the high temperature phase diagram shown in

figure 1. To briefly explain this diagram, consider a crystal grown from a stoichiometric melt at point A on the liquidus. The first composition to solidify is the composition at point B on the solidus at about 49 mole percent Li_2O, leaving the melt richer in Li_2O. A crystal composition close to stoichiometric can be obtained when the initial melt composition is about 58 mole percent rich in Li_2O However, the large difference between the melt and solid composition in this case leads to great difficulty in obtaining homogeneous crystals. On the other hand, crystals of uniform composition and high optical quality can be obtained from an initial melt of 48.6 mole per cent Li_2O. These crystals are congruent since both crystal and melt have the same composition at all times during growth.

In $LiNbO_3$, several parameters are relatively sensitive to the crystal composition. These include the ferroelectric Curie temperature [11], the nuclear magnetic resonance (NMR) linewidth of the ^7Li and ^{93}Nb nuclei [12], the birefringence and hence the second harmonic generation phase matching temperature T_{pm} [13], and the Raman spectrum [14]. A range of Curie temperatures from about 1020 to 1185^oC is measured in $LiNbO_3$ as the solid composition is changed from 46 to 50 mole percent Li_2O as shown by the broken line in figure 1 [11].

Nuclear magnetic resonance spectra from the ^7Li and ^{93}Nb nuclei are easily observed in both powders and crystals of $LiNbO_3$ [12]. Because of the large electric quadrupole

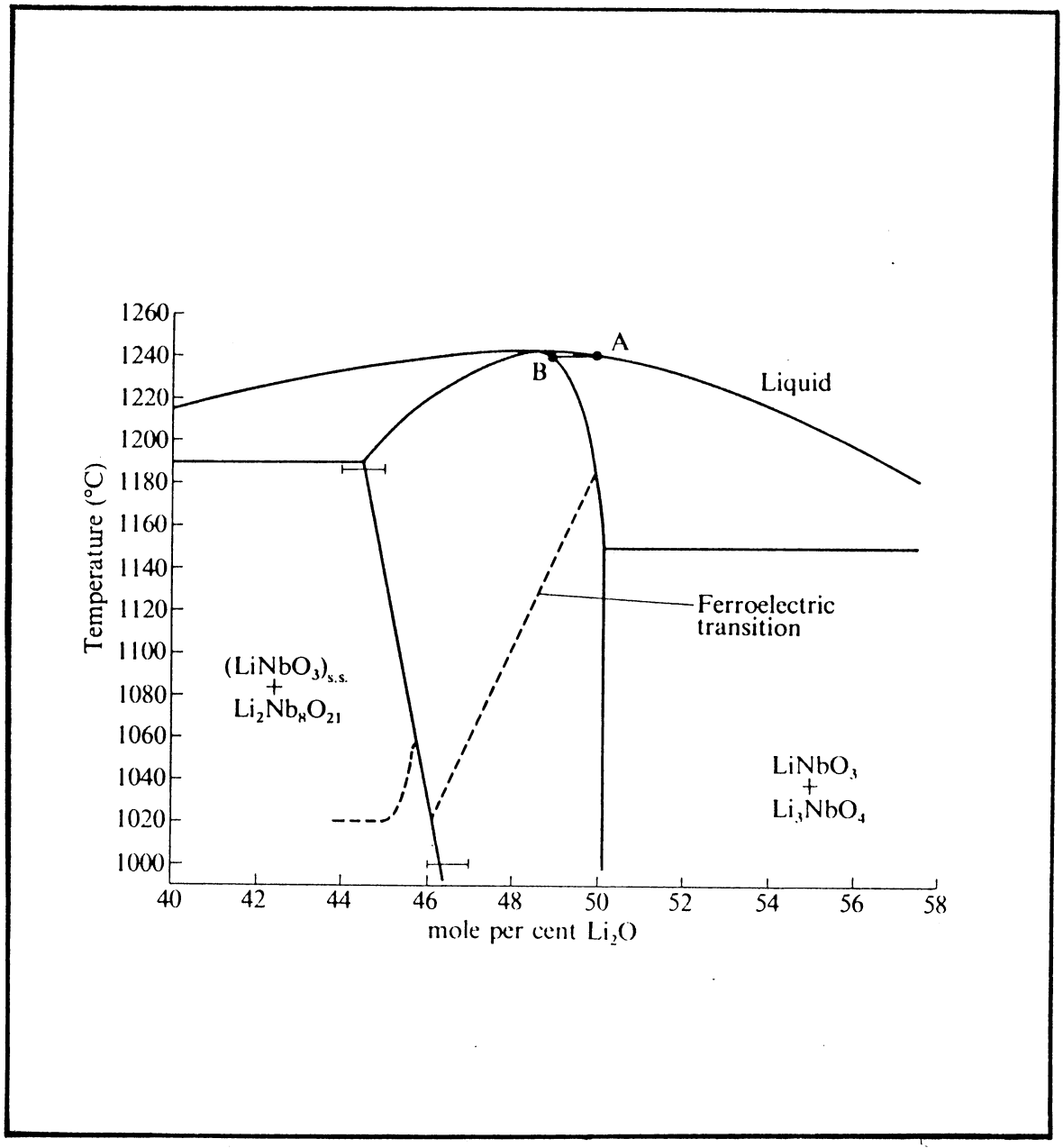

Figure 1. Phase diagram of the Li_2O-Nb_2O_5 system. (after Carruthers et al. [11])

moment of the niobium nucleus, random electric field gradients due to the surrounding charged defects drastically broaden the NMR lines. The experimental results verify that the NMR linewidth is a direct measure of the random defect distribution and, hence, a measure of stoichiometry. The use of Raman spectroscopy similarly relies on the broadening of Raman-active modes which occurs when the translational symmetry of the lattice is reduced in off-stoichiometry crystals.

Crystal Structure

Initially, lithium niobate was thought to have the pervoskite structure. This was later found to be untrue. Determination of the crystal structure of lithium niobate reduces to two problems, identification of one structure above the Curie temperature and identification of a different, lower symmetry structure below the Curie temperature. A definitive structure analysis for the low temperature phase (below T_c) has been reported by Abrahams and coworkers in a series of three papers [6,7,15]. In the first of these papers [6], an x-ray diffraction technique was employed to study the structure of a single crystal of lithium niobate at 24°C. In the second paper [7], they verified their previous results by using neutron diffraction to determine the structure parameters of a single crystal of lithium niobate. A further x-ray diffraction study [15] of $LiNbO_3$ on a polycrystalline sample between 24° and 1200°C

was not as precise as one would wish because of the loss of oxygen from the sample and a tendency of the $LiNbO_3$ to react with the platinum holder at elevated temperatures.

Abrahams et al. [6] determined that the crystal structure below T_c is rhombohedral (space group R3c) with lattice constants $a_H = 0.514829 \pm 2$ nm, and $c_H = 1.38631 \pm 4$ nm. These results were obtained without any reference to earlier works. Furthermore, this was purported to be the first measurement of the absolute configuration of the atomic arrangement in a ferroelectric crystal. The $LiNbO_3$ structure consists of planar sheets of oxygen atoms forming a network of distorted octahedra. Below ferroelectric Curie temperature, the centers of the distorted oxygen octahedra along the c axis are one-third filled by lithium ions, one-third filled by niobium ions, and one-third vacant. The sequence of this arrangement is niobium, vacancy, lithium, niobium, vacancy, lithium, etc. and is shown in figure 2.

The niobium, in its distorted oxygen octahedra, is 0.09 nm from its nearest oxygen layer and 0.141 nm from its next-nearest oxygen layer at 24°C. The corresponding values for lithium are 0.071 nm and 0.16 nm. Both of these configurations are shown in figure 3. At higher temperatures, up to 1000°C, Abrahams, Levinstein, and Reddy [15] could not measure any significant change in the position of lithium ions. However, there was a definite tendency for the niobium ions to approach their oxygen-cage centers as the phase-transition region (T~1200°C) was approached. These results

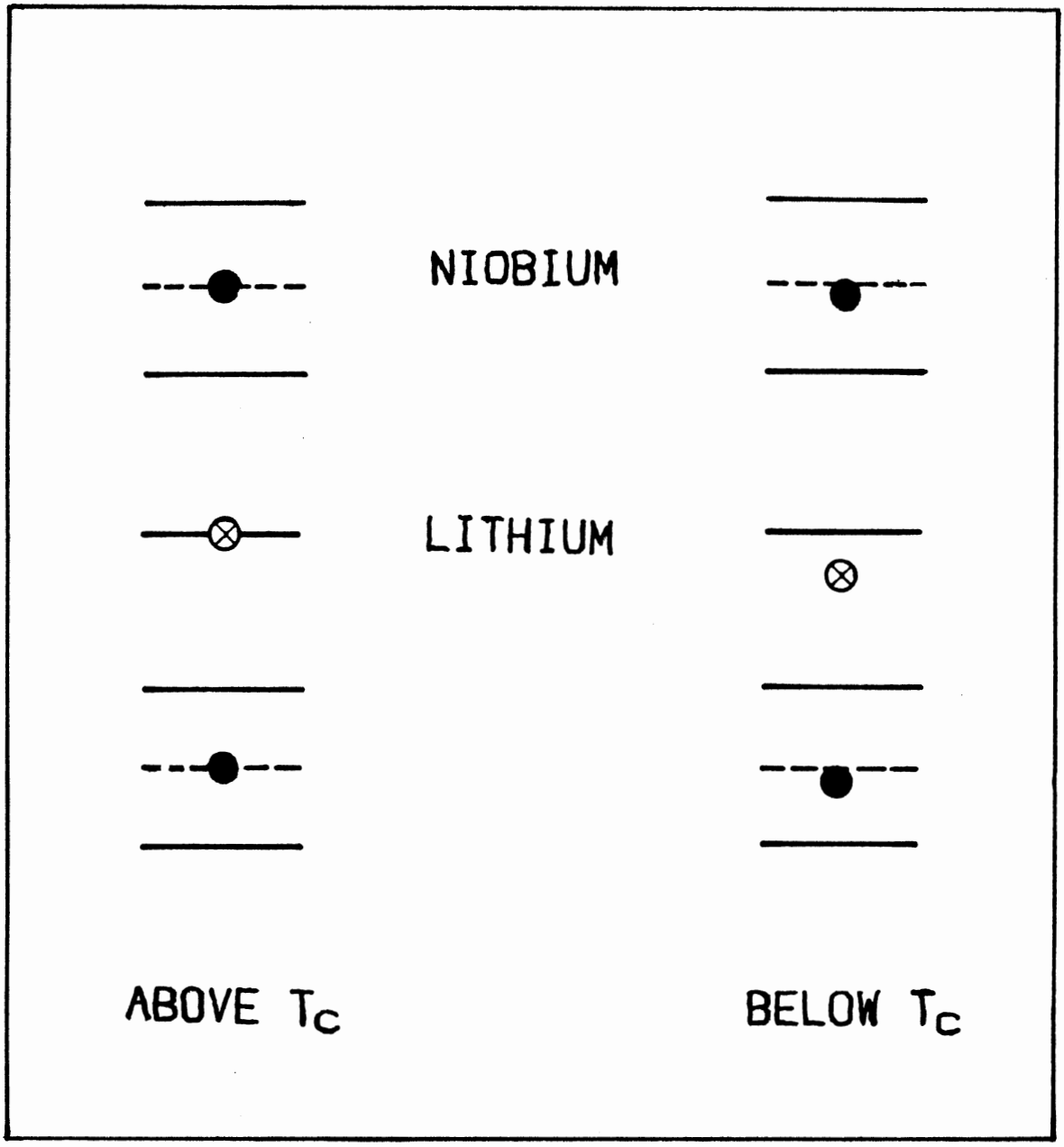

Figure 2. Crystal structure of lithium niobate above and below the Curie temperature.

strongly suggest a centrosymmetric non-polar phase in which the lithium ions move into their nearest oxygen planes and the niobium ions are midway between adjacent oxygen planes as shown in figure 2. A more detailed structural analysis of lithium niobate above its ferroelectric Curie temperature was carried out by Niizeki, Yamada and Toyoda [16]. They found the space group of lithium niobate above the ferroelectric Curie temperature to be $R\bar{3}c$ and the point group to be $\bar{3}m$.

Photorefractive Effect

Laser-induced changes in the refraction indices occur in many ferroelectric materials and is referred to as the photorefractive effect, or "optical damage". The word photorefractive has been accepted for this phenomenon in analogy to "photochromic" which refers to optically induced color change. The photorefractive effect has greatly limited many of the applications of lithium niobate in the visible region of the spectrum. On the other hand, these changes of refraction index induced by laser light may be used to store information via holograms. This "holographic storage" technique has many potential applications.

Refraction index changes induced by lasers were first observed by Ashkin, Boyd, Dziedzic, Smith, Ballman, Levinstein, and Nassau [17] in 1966, although unusual effects observed earlier in 1964 by Peterson et al. [18] can be ascribed to this effect. The index change of the crystal

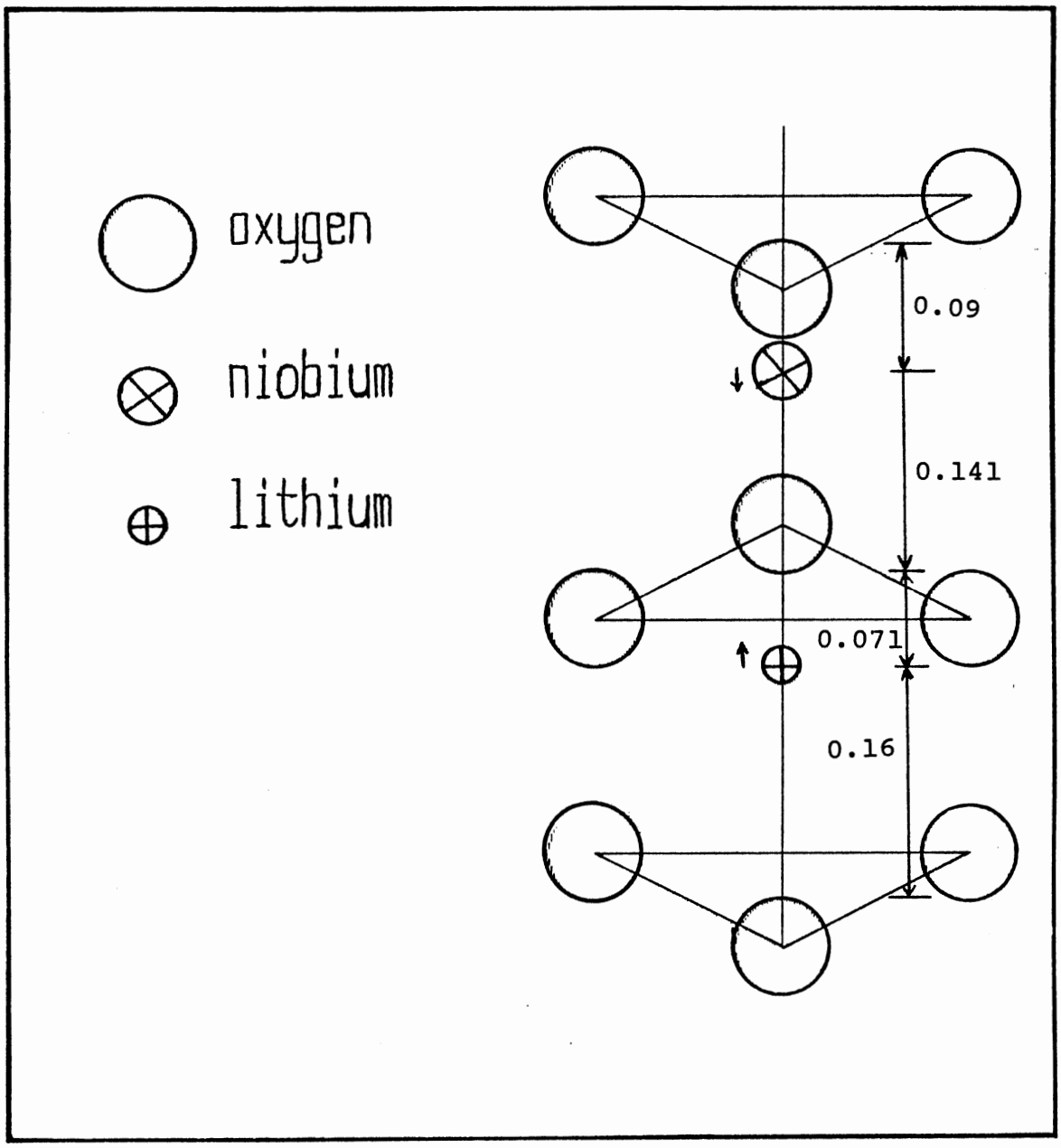

Figure 3. Relative positions of lithium and niobium in oxygen octahedra.

within the region illuminated by the laser distorts the wavefront of the transmitted optical beam and for this reason the effect has been frequently referred to as laser damage, although the origin of the effect is quite different from the catastrophic irreversible damage which occurs at much higher optical intensities. A considerable amount of effort has therefore been devoted to both increasing and decreasing the susceptibility of crystals to these index changes for the various applications.

To explain many of the early observations of the photorefractive phenomenon, Chen [19] in 1969 suggested that this effect was due to the drifting of photoexcited electrons out of the illuminated region followed by their re-trapping near the beam periphery. The electric space charge field established between these re-trapped electrons and the ionized positively charged centers in the illuminated region causes the observed change of refractive indices via the linear electro-optic effect in the crystal.

In his proposed model, Chen [19] assumed there were two types of electron traps present in the as-grown crystal. Traps of the first type are initially filled and are neutral, they provide electrons by photoexcitation. Traps of the second type are initially empty and can capture electrons. Chen also assumed that there is an initial intrinsic electric field in the direction of the spontaneous polarization of the sample, i.e., from the positive to the negative end of the crystal along the c axis. The photoexcited elec-

trons drift toward the positive end of the spontaneous polarization leaving behind positively charged ionized trap centers. The photoexcited charges will be continuously retrapped and then re-excited out of the traps until they eventually drift away from the illuminated region. For deep traps, the thermal excitation is too weak to re-excite charges out of the traps, and the negative charges remain semi-permanently trapped there.

The electric space charge field, E_s, thus created between the trapped electrons and the positive ionized centers cause the observed spatial variation of the indices of refraction via the electro-optic effect of the sample. Furthermore, since lithium niobate shows a linear electro-optic effect, i.e., an external electric field applied in the direction of the spontaneous polarization, P_s, of the samples decreases (n_e-n_o) linearly and a field applied opposite to P_s increases (n_e-n_o) linearly along the c axis, the observed spatial variation of change in (n_e-n_o) is linearly related to the spatial distribution of electric field. A spatial distribution of trapped electrons and positive ionized centers which gives rise to the observed spatial distribution of refraction index changes in the region illuminated by laser beam builds a space-charge field which is in the right direction to decrease the change in (n_e-n_o) near the beam spot, and hence diverge the laser beam. Also, it is consistent with the observation that the change in (n_e-n_o) along the c axis reverses sign near the beam edge

but it remains negative since the space charge field (and hence the magnitude of change in (n_e-n_o)) is larger (for long exposure time) near the positive c side of the beam edge. The induced index change results mainly in the distortion of the extraordinary index because the field induced change (electro-optic effect) of the extraordinary index is larger than the change of the ordinary index by approximately a factor of four when the field is along the c axis as described by Lenzo et al. [20] and Turner [21] in 1966.

Chen's model for the photorefractive effect, as described above, explains the observed spatial distribution of optically induced refraction index changes. To account for a change in (n_e-n_o) of approximatly 10^{-3} via the electro-optic effect, Chen [19] calculated that a space-charge field of 6.7×10^4 V/cm would be needed. The density of photo-excited electrons required to produce such a field was estimated by assuming two cylinders of 0.1 mm diameter (the beam diameter used to obtain data) are in contact and one of them is charged uniformly with positive charges while the other is charged with negative charges. Then an electron density of approximately 4×10^{14} per cm^3 would be required to produce an electric field of 6.7×10^4 V/cm at the contact.

Erasing of the induced refractive index changes by flooding the sample with UV light or heating above 170^oC was explained by Chen [19] in the following way. Flooding the sample with a large diameter light beam from a UV source causes the trapped charges outside the boundary of the orig-

inally illuminated region as well as the charges in the non-ionized trap centers to be photoexcited. These charges drift out of the region flooded by the ultraviolet and become re-trapped at the periphery of the erasing UV beam, thus creating a new larger area of index changes. The index changes in the small originally illuminated region is effectively erased because the trapped charges immediately outside of its initial boundary are removed.

In the thermal erasing method, the sample is heated above 170^{o}C for a brief period of time. During this process, the trapped charges are thermally excited to the conduction band. The optically induced index changes disappear because the conduction electrons drift back to the illuminated region where they neutralize the positive ionized centers.

In his proposed model for the photofractive effect as discussed above, Chen [19] did not specify the identity of the various traps in $LiNbO_3$, although he did suggest that the oxygen vacancy might be a possible candidate for the source of photoexcited electrons. Nevertheless, without a clear understanding of either the absorbing and trapping defects or the origin of the internal field, Chen demonstrated how the photorefractive effect can be used as the basis of a volume holographic information storage device of extremely high bit density. In the years since Chen's initial study, a great deal of effort has been devoted to identifying the microscopic details of the photorefractive mechan-

isms in order to optimize $LiNbO_3$ crystals for memory, nonlinear, and integrated optics applications.

Following the work of Chen, Johnston [22] was the next investigator to examine the mechanisms respnsible for the photorefractive effect. The large spontaneous crystal field required by Chen's model was difficult to account for since it was too large to be due to the pyroelectric effect. However, Johnston pointed out that no initial internal field is required for the photorefractive effect. Optical excitation of a pyroelectric crystal gives rise to a macroscopic polarization change in the illuminated region and the divergence of this polarization acts as a source for an electric field. This polarization gives an index change via the electrooptic effect. In this way, Johnston showed that the distribution of trapped carriers resulting from the diffusion of conduction electrons was skewed by the electric field produced by the divergence of the polarization. This was able to account for all the details of Chen's observations (which Chen's model could not) without requiring any internal fields before or after illumination of the crystal. Johnston also removed the requirement in Chen's model for a crystal resistivity sufficiently high that the space charge field remained for extended periods (on the order of weeks).

Further investigation of the responsible defects for the photorefractive effect in electro-optic crystals by Glass et al. [23] in 1972 revealed that Fe^{3+}/Fe^{2+} ions play a dominant role in the optical index changes of the crystals

via electro-optic effects. They varied the stoichiometry of the $LiNbO_3$ and showed that the defects resulting from stoichiometric changes were not the origins of the photorefractive phenomenon. Results from heat treatments, impurity and color center content, results from x-irradiations, and the kinetics of index damage processes were all accounted for by Fe^{2+} ions to Fe^{3+} ions conversions. By employing an electron spin resonance spectrometer operating at 512 MHz, traces of Fe^{3+} were found in nominally pure crystals with concentration of 10 to 100 ppm.

In order to control and reduce the phototrefractive effect in the crystals of $LiNbO_3$, the addition of colorless impurities such as Ti^{4+}, W^{6+}, Mg^{2+}, and Al^{3+} ions to stabilize the trivalent charge state of iron (Fe^{3+} ions) was attempted [23]. Although these impurity dopings didn't prove very successful at the time, they provided a foundation for further characterization and understanding of the responsible defects for the photorefractive effect. They allowed later investigators to prepare materials having a high photorefractive sensitivity for holographic recording which were comparable with the sensitivity of silver halide emulsions. Also, they allowed materials to be developed in which the photorefractive sensitivity was either very low or, in some cases, too small to measure.

There is no doubt that the simple picture of Fe^{2+}/Fe^{3+} conversions accounts for the observed photorefractive effects in undoped commercial $LiNbO_3$ crystals as well as iron-

doped $LiNbO_3$ crystals. Also, this Fe^{2+}/Fe^{3+} conversion satisfies the requirements of Chen's model for appropriate source and trapping sites. However, it must be emphasized that other absorbing centers which can be photoionized with light of the proper wavelength will also in general give rise to a photorefractive effect provided the appropriate trapping sites are available. Indeed, Phillips et al. [24] demonstrated how other multivalent impurities such as Cu^{1+}/Cu^{2+} and Mn^{2+}/Mn^{3+} conversions also give rise to an increased damage susceptibility. In different spectral regions or different materials, other absorption mechanisms associated with other multivalent impurities may prove to be even more effective.

Glass [25], in a review of the photorefractive effect, evaluated the mechanisms responsible for this effect in electro-optic crystals destined for applications such as optical memories, holographic interferometry, and integrated optics. He pointed out that iron impurities were present in undoped $LiNbO_3$ crystals at concentrations typically in the 1-10 ppm range or greater. In referring to his previous work, Glass reviewed attempts to obtain damage-free crystals including the growing of high-purity crystals and the heat treating of crystals at low temperatures ($<600^{o}C$) for long periods of time in an oxygen atmosphere. While these attempts resulted in significant improvements, they did not result in damage-free crystals. From measurements of the photorefractive effect in various $LiNbO_3$ crystals, Glass

[25] estimated that concentrations at or below 0.001 ppm of Fe^{2+} ions would be necessary to eliminate the effect for most applications. Other possible mechanisms to explain the photorefractive effect such as two-photon absorption, two-step absorption, and a transport mechanism were discussed by Glass [25].

A major step in improving the resistance of $LiNbO_3$ to optical damage came about when Bryan et al. [26] reported significant changes in the observed photorefractive effect if more than 4.5% MgO is added to the melt during crystal growth. Their systematic investigation included crystals with a variety of Mg-doping levels and with different Li/Nb ratios, and they demonstrated the existence of a threshold effect with regard to Mg doping level. Bryan et al. [26] also measured a significant increase in the photo-conductivity of Mg-doped $LiNbO_3$ crystals. They suggested that the improved performance was due to this significant increase in photoconductivity. In the present dissertation, it is shown that the presence of magnesium at high concentrations in $LiNbO_3$ crystals disturbs the Fe ions significantly, thus allowing the majority of Fe^{3+} ions to enter $LiNbO_3$:Mg in a different environment. The new environment of the Fe^{3+} ions produces a different ESR spectrum different from that observed from Fe^{3+} ions when magnesium is not present.

Improved extinction ratios and operation at higher power densities are achieved in devices fabricated from $LiNbO_3$ crystals that are heavily-doped with magnesium.

Further characterization of point defects in Mg-doped lithium niobate was carried out by Sweeney et al. [27]. Spectroscopic techniques including x-ray-induced luminescence, optical absorption, and electron spin resonance were employed to characterize the reduction and radiation properties of Mg-doped lithium niobate crystals. Different Mg-doping levels and different Li/Nb ratios were compared to undoped materials. Sweeney et al. [27] reported the observation of a thermoluminesence peak near 70 K, an optical absorption band peaking at 1200 nm, and a broad ESR spectrum at g_c = 1.82. Possible models for the responsible defects were suggested and elaborated.

CHAPTER II

EXPERIMENTAL PROCEDURE

Introduction

In this chapter, we will describe the various instruments and procedures utilized in the course of this investigation. First, we will specify the origin of the samples and describe which samples were used in each experiment. This is followed by brief descriptions of the specific optical absorption, electron spin resonance (ESR), and electron-nuclear double resonance (ENDOR) spectrometers used. Finally the sample treatments such as reduction, radiation, and thermal anneals at various temperatures are described.

Samples

A variety of undoped and doped lithium niobate samples were used in this study. These samples were cut from $LiNbO_3$ boules obtained from three different sources. One set of undoped samples was used for room-temperature irradiation. From the same boule, another set of samples was reduced at high temperature and their response to optical bleaching at 77 K was studied. This boule was obtained from Union Carbide, Washougal, WA. The company specified this boule to be their nominally pure acoustic grade.

A second group of commercial samples, co-doped with magnesium and iron, were used for the characterization of iron, as perturbed by the presence of magnesium, in lithium niobate. These boules were grown for McDonnell Douglas by Crystal Technology, Palo Alto, CA. Each boule in this series had the same level of Mg (5% MgO in the melt), but different amounts of iron. One set of samples had 100 ppm iron and the other set had 200 ppm iron, nominally.

A third group of samples were doped with titanium (in the melt) and then used in experiments to characterize the behavior of the titanium ions in the lithium niobate lattice. These Ti-doped samples were cut from a boule grown in the Crystal Growth Laboratory at Oklahoma State University. This boule was pulled from a congruent lithium niobate melt to which 1% TiO_2 (by weight) had been added. The lithium niobate and the titanium oxide powders were purchased from Johnson-Matthey, the pulling rate was 0.5 cm/hr, and the pulling rod rotated at a rate of 2.8 rpm during the growth. This boule was not subjected to any post-growth treatment such as oxidation or poling of the crystal.

The samples for the visible and infrared absorption experiments were cut to typical dimensions of 10 x 15 x 2 mm^3 using a diamond saw. They were then polished to an optical quality surface using Buehler, Ltd. silicon carbide powder and 9, 7, and 3 micron diamond paste.

Optical Apparatus

Our optical absorption data were taken using a Perkin-Elmer Model 330 spectrophotometer. This is a double-beam instrument which covers the spectral range from 185 nm to 2600 nm. The resulting spectra were stored by the Perkin-Elmer 3600 data acquisition computer interfaced to the spectrophotometer. For optical absorption measurements below room temperature, we used a liquid-nitrogen cryostat constructed in the Instrument Shop at Oklahoma State University. A diagram of this cryostat is provided in Figure 4. The operating range for this instrument was between 85 and 300 K.

Sequential annealing of a sample initially irradiated at 85 K was accomplished by blowing all the liquid nitrogen out of the above-described cryostat and then inserting a cartridge-type heating element into the cryostat's well. The voltage across the heater was adjusted by a Variac to achieve the desired temperature. To maintain this temperature, a small amount of liquid nitrogen would be added in the case of over-shoot. During sequential anneals, the sample was heated to the desired temperature, the temperature was then maintained at that value for a given period, and finally the sample was cooled back to the base temperature for measurement. The entire procedure was then repeated at the next higher anneal temperature. This technique allowed us to correlate the behavior of ESR and optical absorption spectra.

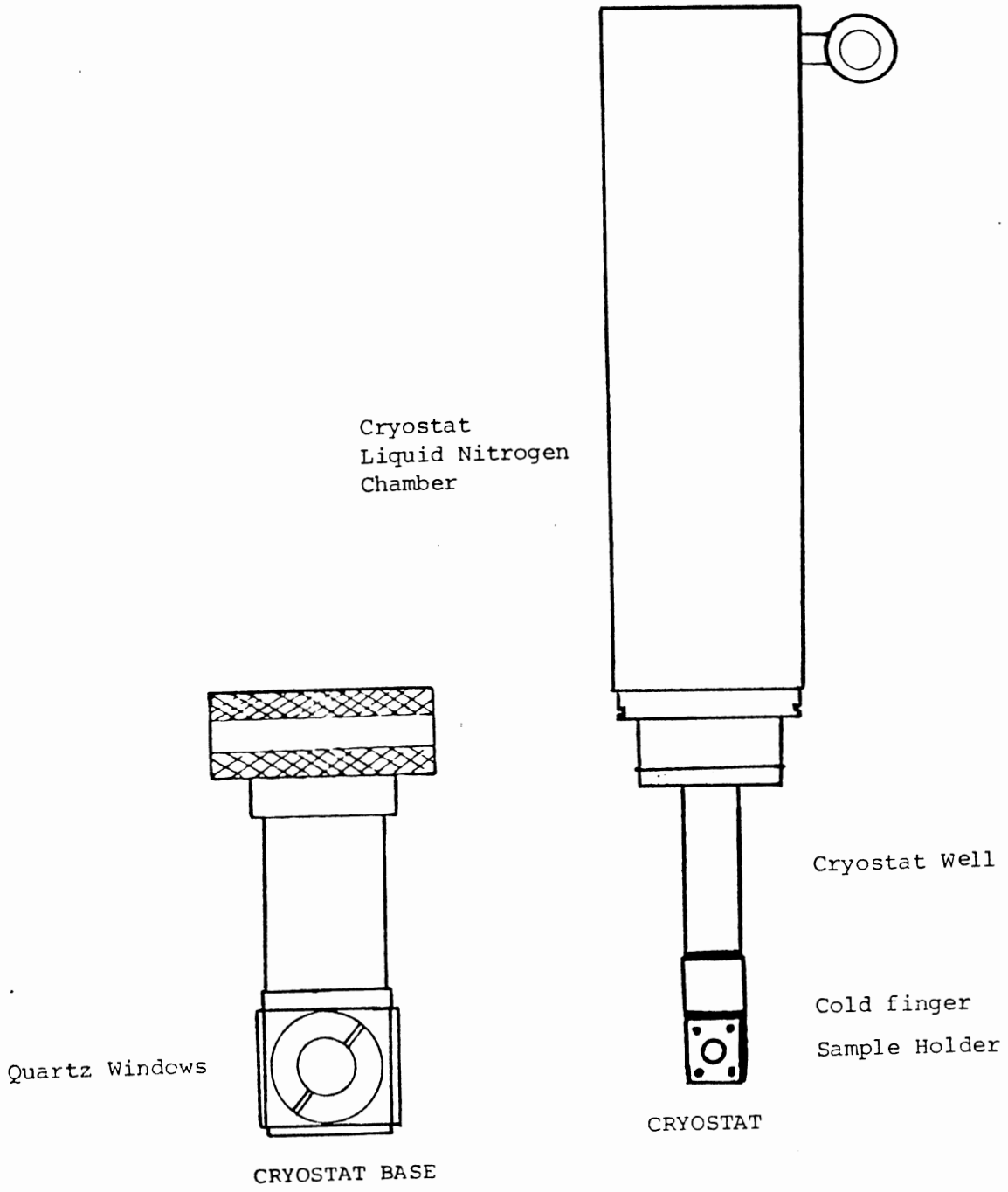

Figure 4. A diagram of the optical cryostat.

Infrared absorption measurements were made using a double-beam Beckman 4240 spectrophotometer, which operated from 4000 to 250 cm^{-1}. All the infrared absorption data reported in this dissertation were taken at room temperature.

ESR and ENDOR Apparatus

Electron spin resonance (ESR) measurements were carried out using a Varian 4501A spectrometer or a Bruker ER-200D SRC spectrometer. The Varian spectrometer operated at a microwave frequency of 35 GHz (Ka band) and used special tapered pole caps on the magnet to achieve the necessary high magnetic fields (10 to 17 kG). The Bruker spectrometer operated at microwave frequencies near 9.4 GHz (X band). Both ESR spectrometers had a 100 kHz static field modulation.

ESR measurement at 77 K were made possible by using the quartz finger Dewar shown in figure 5. This Dewar was constructed by personnel in the Glass Shop at Oklahoma State University. The finger Dewar consisted of a double wall quartz tube with a vacuum in between for thermal isolation. The Dewar could be positioned such that its tail extended into the microwave cavity. This allowed the sample to be directly placed in the liquid nitrogen during measurements.

A Bruker nitrogen gas flow system was used for thermal anneals performed outside the microwave cavity. Although this nitrogen gas flow system was originally designed to fit

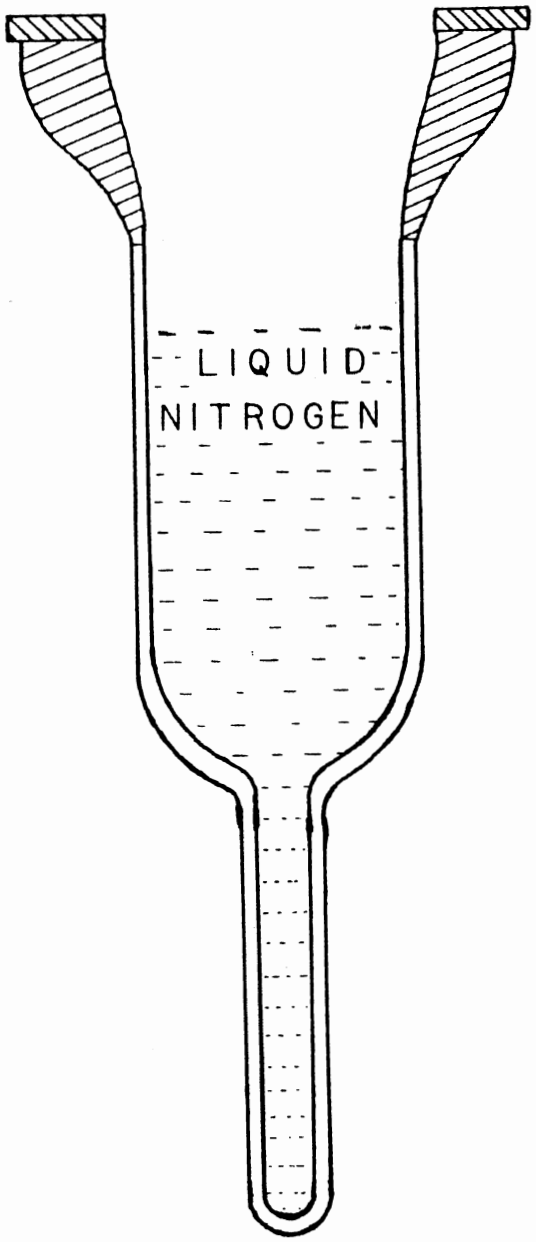

Figure 5. A diagram of the ESR finger Dewar.

inside the microwave cavity and be used for variable temperature measurements, the previously described home-built quartz finger Dewar proved to be more versatile for all measurements at 77 K because it ensured a consistent sample temperature. Controlled temperatures between 80 K and 300 K were possible with the Bruker gas flow system. Sample sizes were typically 2 x 2.5 x 8 mm^3 for ESR measurements with the X-Band bridge, and 1 x 1.5 x 8 mm^3 for ESR measurements with the Ka-Band microwave bridge.

Electron nuclear double resonance (ENDOR) measurements were made using the above-described Bruker ER200D ESR spectrometer. The Bruker Model 250 ENDOR accessory was added to the ESR system. It consisted of a special ENDOR cavity, an Aspect 2000 computer, various ENDOR interfaces to the ESR spectrometer, an rf signal generator, and a 200-W rf amplifier. Figure 6 shows a simplified block diagram of the ENDOR system. The ENDOR cavity produces a microwave magnetic field at the sample which excites electron spin transitions, and it also supplies an rf magnetic field at the sample. The ENDOR cavity thus is an ESR cavity with the additional capability of delivering rf magnetic fields to the sample. The rf magnetic field is supplied by an rf helix mounted on a quartz variable temperature Dewar inserted into the microwave cavity. This cavity resonates in the TM_{110} mode. The rf helix in the Bruker cavity allowed for a broad-band operation from 0.5 to 100 MHz as well as rf frequency modulation depths of up to 500 kHz. The ENDOR sample

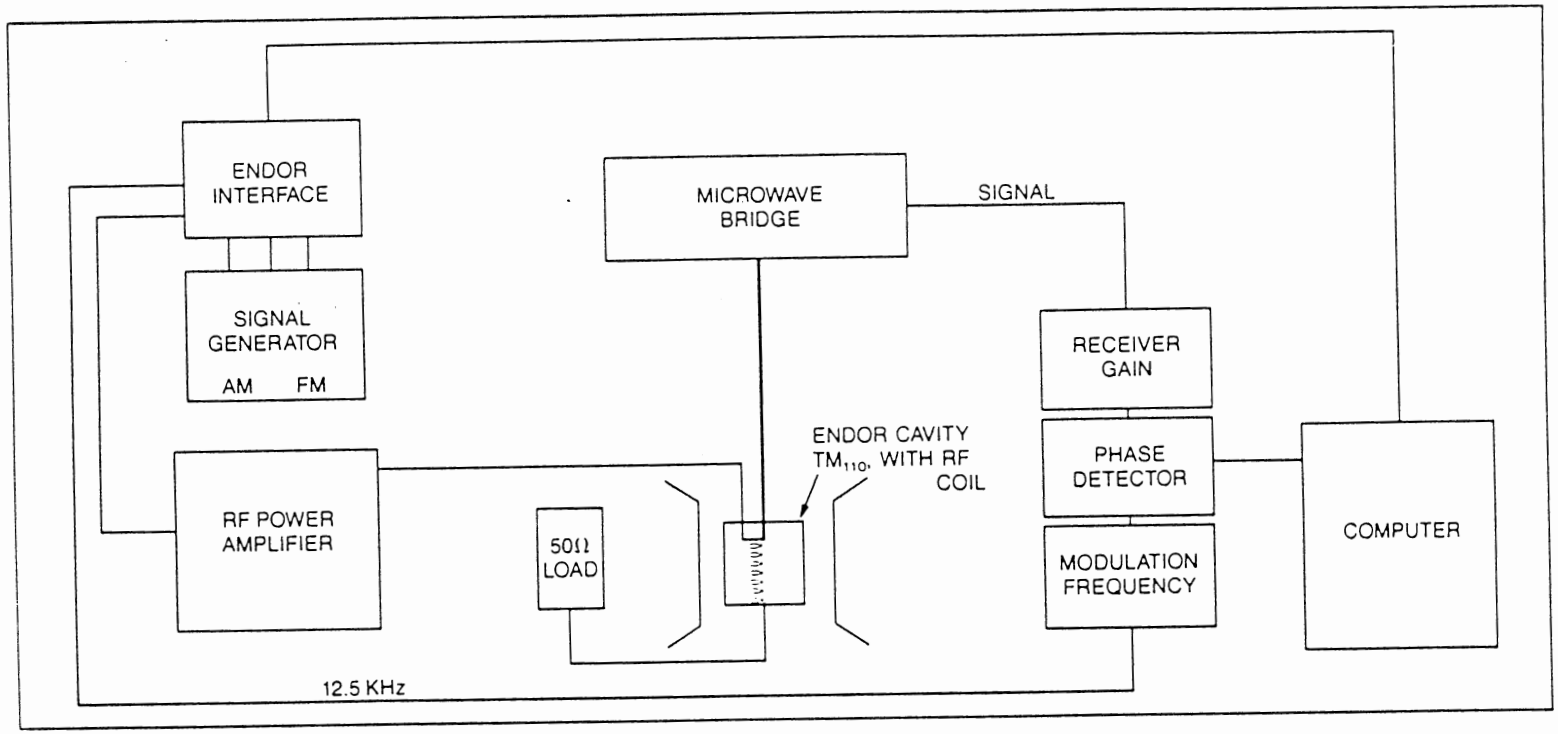

Figure 6. Block diagram for the ENDOR spectrometer.

was cooled by an Oxford ESR-900 continuous flow cryostat which provides a continuously variable sample temperature in the range 4 K to 300 K. Liquid helium was delivered to the cryostat through an Oxford GFS-300 transfer tube. The temperature of the sample was monitored and controlled by a Model TC1 Oxford Temperature Control unit.

Reduction Treatments

Optical and ESR samples were reduced by heating in an oxygen-deficient atmosphere. A Hoskins tube furnace capable of temperatures up to 1250^{o}C was used. The furnace temperature was controlled by an Omega Microprocessor-Based Temperature Controller Model 6050. The samples were placed inside a small stainless steel tube chamber with a Chromel-Alumel thermocouple extending inside it. The small stainless steel tube chamber was then inserted into a larger diameter stainless-steel tube which passed through the furnace. The stainless-steel tube was then evacuated to a pressure of 10^{-5} torr or less. The stainless steel tube was then flushed three times with argon gas. The stainless-steel tube was finally filled with argon gas to a pressure of approximately 0.9 atmospheres and the furnace was turned on to reduce the samples at the desired temperature.

Radiation Treatments

A 2-Mev Van de Graaff accelerator operating in the electron mode was used to produce defects in the ESR and

optical samples used in this study. The samples of $LiNbO_3$ would crack when placed directly in the electron beam for a period longer than 30 seconds. Since the crystals are ferroelectric, presumably the cracking was caused by the high electric fields generated by the build-up of charge on the internal surfaces of the crystal. However, this cracking could be minimized by placing the samples at a distance of about 60 cm from the Van de Graaff's aluminum exit window during the irradiations and by keeping the intervals of irradiation times below 30 seconds.

The other procedure employed during irradiation was to produce x-rays by scattering the Van de Graaff's high-energy electrons from a copper block. The samples were placed in the path of the x-rays at a distance of about 10 cm from the copper block.

Thermal Anneals

Sequential annealing of the $LiNbO_3$ samples above room temperature were carried out via a small portable oven constructed in the Instrument Shop at Oklahoma State University. The oven consisted of a small copper housing with a heating element wrapped around it and a Chromel-Alumel thermocouple placed inside the copper housing to monitor the temperature. The input voltage across the heater was regulated by an Omega Microprocessor-Based Temperature Controller Model 6051. The operating range of this oven was from room temperature up to 550^{o}C. The auto-tune feature of the

Omega Temperature Controller allowed a fine temperature adjustment upon reaching the set point within $\pm 1^{o}C$ of the set point.

CHAPTER III

EXPERIMENTAL RESULTS AND DISCUSSION

Introduction

The experimental results of this investigation are presented and discussed in this chapter. First, results from the room-temperature irradiation of undoped samples of $LiNbO_3$ are presented and the correlations between the optical absorption and the ESR spectra observed before and after irradiation are discussed. Second, the effects of optical bleaching at 77 K on a sequentially reduced sample of $LiNbO_3$ are presented and possible explanations of these observations are provided. Third, the results obtained from the characterization of iron in crystals of lithium niobate co-doped with magnesium are described. This work also involved a sample which was sequentially reduced at progressively higher temperatures. Next, the ESR and optical spectra of $LiNbO_3$:Ti crystals taken after various reduction and radiation treatments are presented and possible models for the responsible defects are suggested. Finally, the ENDOR results obtained from various samples of lithium niobate are presented and possible interpretations are given.

Room-Temperature Irradiation of $LiNbO_3$

Room-temperature irradiation turns lithium niobate brown. The brown coloration is the result of a broad absorption band in the visible region of the spectrum. This room-temperature-radiation-induced absorption band has been reported [28] previously, but not identified. In an investigation of optical index damage in electro-optic crystals by Glass et al. [23] in 1972, the divalent iron (Fe^{2+}) ions were suggested to be the responsible defect for the room-temperature-radiation-induced absorption band. In our present investigation, electron spin resonance (ESR) and optical absorption techniques have been used to further characterize the defects responsible for this brown coloration in room-temperature-irradiated $LiNbO_3$.

Figure 7 shows the ESR spectrum of an undoped $LiNbO_3$ crystal before and after exposure to x-ray radiation at room temperature. Both spectra were taken at 77 K with the magnetic field parallel to the crystal's c axis. To facilitate a comparison between the two spectra in figure 7, the spectrometer's gain and microwave power level were kept at the same values for each trace. However, the ESR spectrometer's gain for the ESR transition at about 3000 gauss in trace (b) had to be reduced 4 times. The microwave frequency was 9.30 GHz and the magnetic field was swept from 500 to 5500 gauss. The total dose received by the sample during this x-irradiation was approximately 1 Mrad (Si).

Trace (a) in figure 7 is the ESR spectrum of the $LiNbO_3$

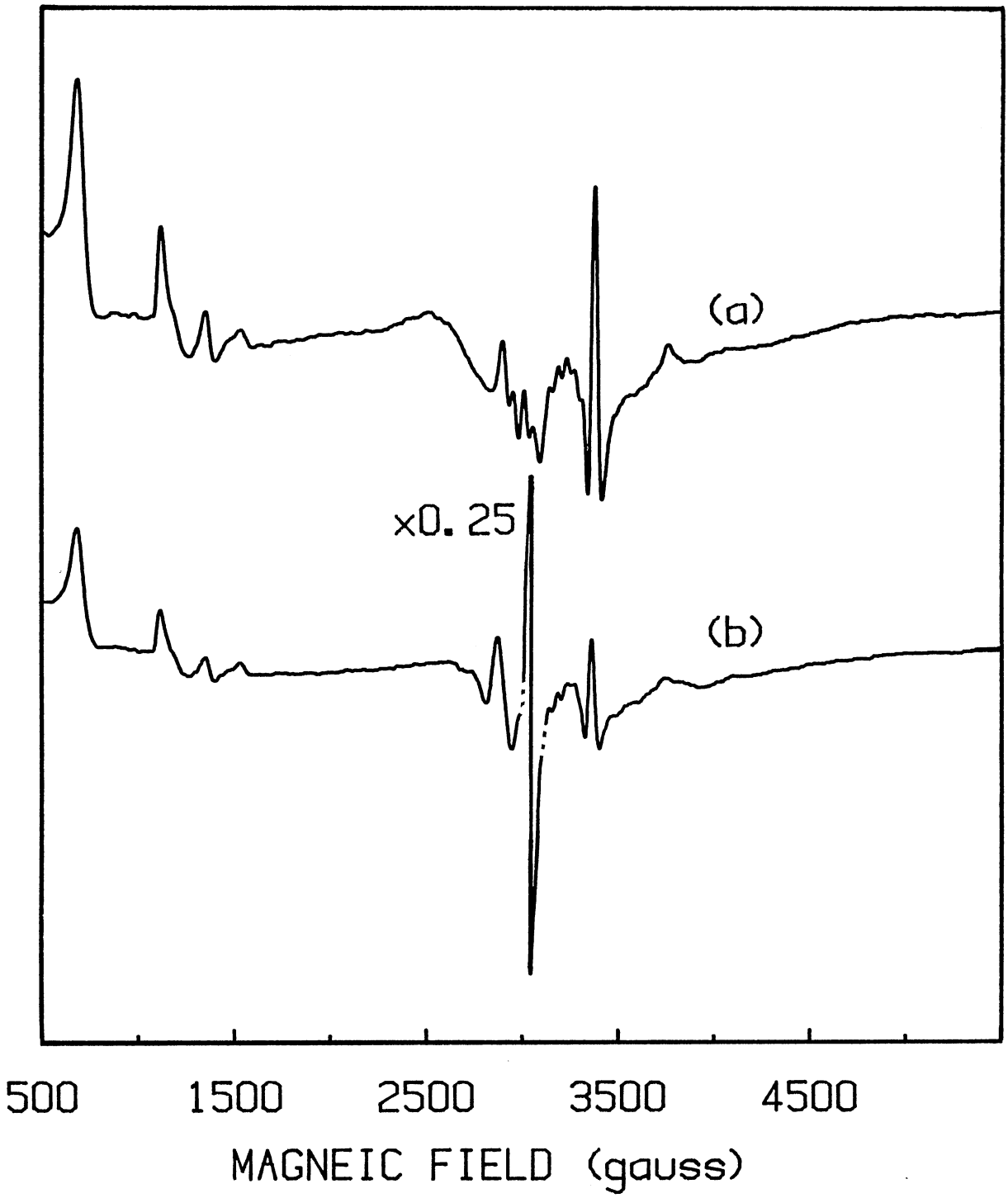

Figure 7. 77-K ESR spectra from undoped $LiNbO_3$. Trace (a) was taken before and trace (b) after a room-temperature irradiation.

crystal before irradiation. The dominant line in this spectrum is at 790 G and it has been previously attributed to Fe^{3+} ions [29-31]. Other ESR lines, with reduced intensity, arising from Fe^{3+} and Mn^{2+} ions are present in trace (a), but these are not of primary concern for our study. The ESR spectrum of the same $LiNbO_3$ crystal after irradiation is shown in trace (b) of figure 7. It provides two additional pieces of information; one is the decrease in the intensity of the Fe^{3+} spectrum and the other is the appearance of a sharp line at $g_c = 2.18$. The concentration of Fe^{3+} ions was decreased approximately 50% by the room-temperature irradiation, as shown in figure 7 (b).

The sharp ESR line at $g_c = 2.18$ has been assigned to nickel [32-34], but there is no clear agreement about which charge state of nickel is being observed after irradiation. Optical absorption investigations of $LiNbO_3$:Ni along with other previous work, have suggested that nickel enters the lattice during growth as Ni^{2+} ions [35-37]. Arsenev et al. [35] calculated the possible energy states of a $3d^8$ electron configuration (Ni^{2+}) as a function of the Racah parameters B and C and the magnitude of the strength of the internal crystal field, Dq. The best values of B, C, and Dq were found by fitting the calculated data to experimental data. Although the value of C they obtained was higher than expected theoretically, the agreement between experimental and calculated data was deemed satisfactory.

In both Ni-doped and undoped samples of $LiNbO_3$, no ESR

spectrum due to Ni^{2+} ions has been reported. This is not surprising since the fast spin-lattice relaxation of divalent nickel ions would be expected to cause the resonance lines to broaden beyond recognition. The new paramagnetic center at $g_c = 2.18$ formed by the room-temperature irradiation could be due to either Ni^{3+} ions (d^7) or Ni^{+} ions (d^9). While Ni^{+} is always an S = 1/2 ion, Ni^{3+} can either be an S = 3/2 or S = 1/2 ion in an octahedral environment, depending on whether the crystal field is weak or strong. Rosa et al. [33] favor the trivalent charge state of nickel. They assumed a strong crystal field in their analysis, and they noted the similarity of g values of Ni^{3+} ions in $SrTiO_3$, TiO_2, and $LiNbO_3$. Korradi et al. [34], on the other hand, suggested that the monovalent charge state of nickel ions would occur after room-temperature irradiation. They based their conclusion on an analysis of the Tanabe-Sugano diagram.

Optical absorption spectra taken at room temperature from an undoped $LiNbO_3$ crystal are shown in figure 8. The absorption spectrum represented by trace (a) was taken before a room-temperature x-irradiation. The absorption spectrum taken after a room temperature x-irradiation (trace b) contains a broad band covering most of the visible region. Our analysis of experimental data suggest that divalent iron (Fe^{2+}) ions are responsible for this broad absorption. A similar absorption band is observed in reduced $LiNbO_3$ samples and the explanation in that case has been one of con-

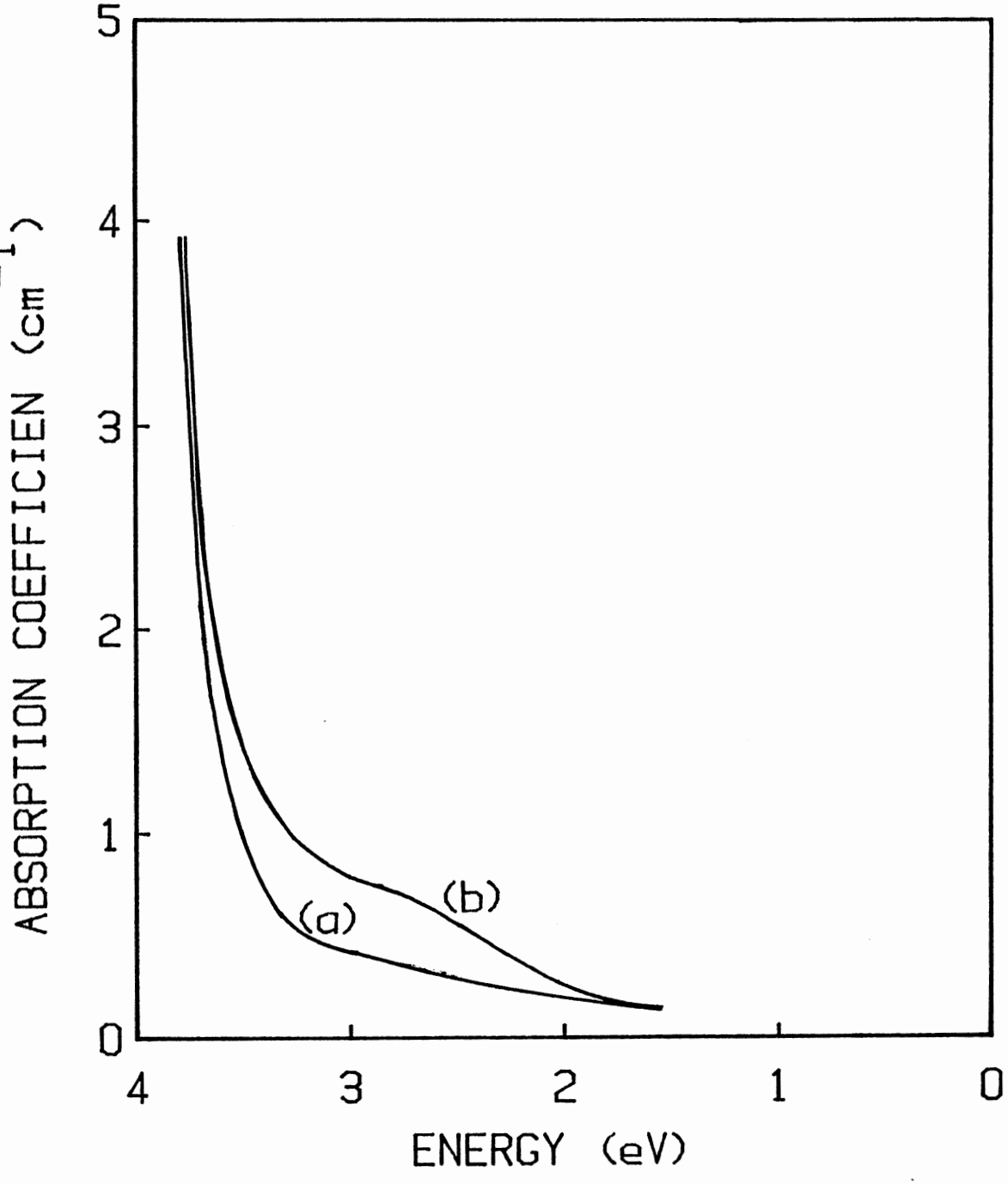

Figure 8. Optical absorption of undoped $LiNbO_3$. Trace (a) was taken before and trace (b) after a room-temperature irradiation.

verting Fe^{3+} ions to Fe^{2+} ions [23]. Although the presence of Fe^{2+} ions and Fe^{3+} ions in $LiNbO_3$ has been verified by Mossbauer spectroscopy, the observation of Fe^{2+} ions by means of conventional ESR is very difficult. Homogeneous broadening, due to a rapid spin-lattice relaxation, prevents the observation of ESR signals from Fe^{2+} ions. Bukharaev et al. [38] have reported observing Fe^{2+} ions by means of acoustic ESR during their investigation of the effect of oxidation and reduction on a series of $LiNbO_3$:Fe samples.

To establish a correlation between the ESR spectra in figure 7 and the optical absorption spectra in figure 8, we investigated the behavior of the responsible defects during thermal annealing experiments. Figure 9 shows the results of a series of pulse anneals following room-temperature x-irradiations. Each anneal step consisted of holding the sample for 5 minutes at the desired temperature and then returning to room temperature (in the case of the optical absorption) or to 77 K (in the case of the ESR) where the intensity of the corresponding defect spectrum was monitored. These sequential sets of annealing data were taken in 20-degree steps from room temperature up to 300°C. Trace (a) in figure 9 shows the decrease in the intensity of the radiation-induced optical absorption band at 500 nm during the pulse anneals, trace (b) shows the increase in the intensity of the Fe^{3+} ESR spectrum during the pulse anneal, and trace (c) shows the decrease in the intensity of the nickel ESR spectrum during the same anneal. The experimen-

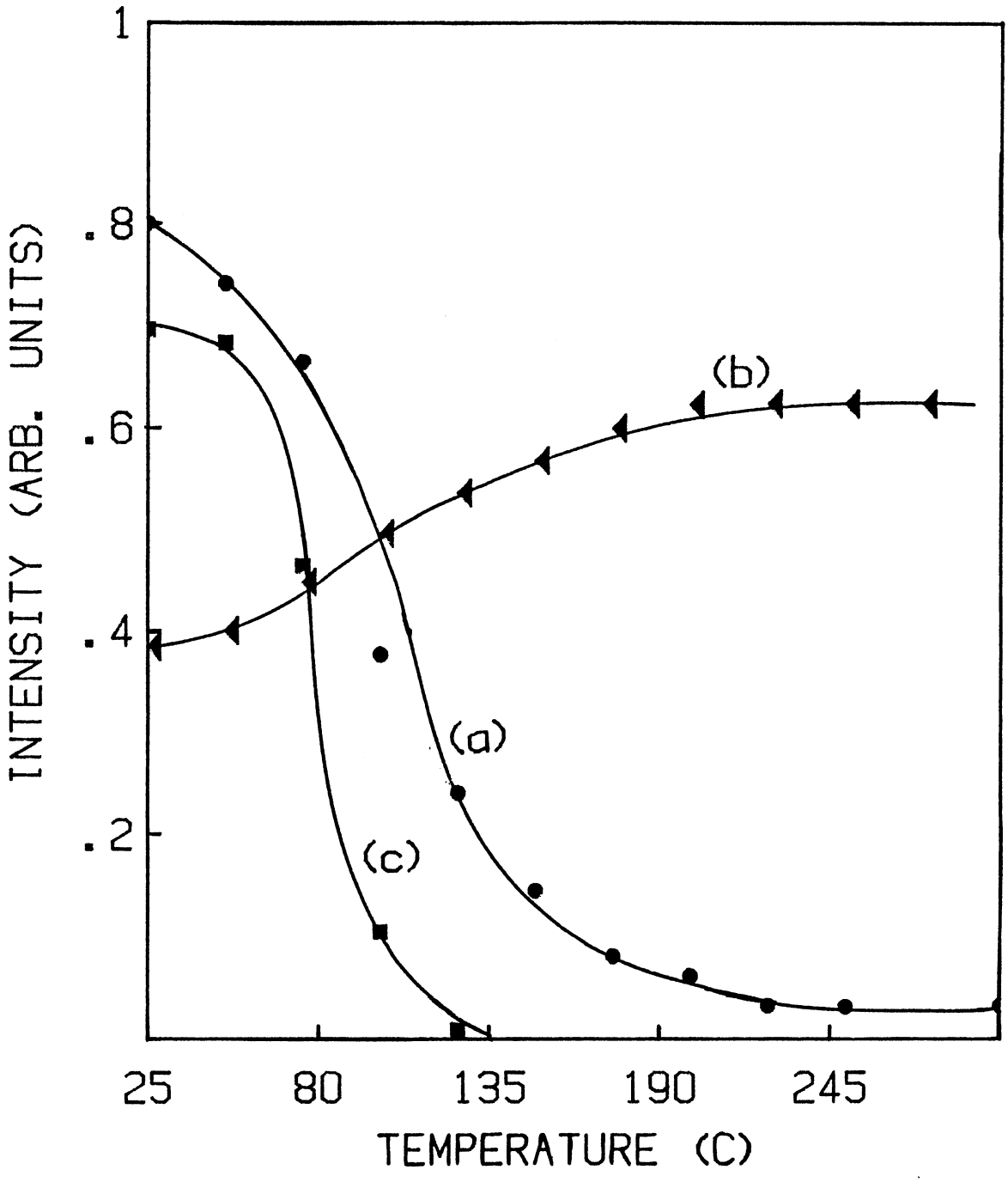

Figure 9. Pulse anneal results from undoped $LiNbO_3$.

tal conditions were kept as similar as possible during the anneals of the optical band and the ESR spectra. We conclude from the plotted intensities of ESR and optical absorption results vs. anneal temperature, in figure 9, that the simultaneous decay of the 500-nm optical absorption band in figure 8 and the changes in the intensity of the ESR spectra of nickel and Fe^{3+} ions of figure 7(b) are correlated.

The experimental results obtained from room-temperature-irradiated $LiNbO_3$ samples suggest at least two possible defect models for these processes. One of the possibilities is based on the assumption of a trivalent charge valency for nickel (Ni^{3+} ions) after exposure to room-temperature ionizing radiation. The x-irradiation would excite an electron from a Ni^{2+} ion into the conduction band thus producing a Ni^{3+} ion. This ionized electron would drift or diffuse along the c axis until it became trapped at an Fe^{3+} ion, thus converting the Fe^{3+} ion into an Fe^{2+} ion. In the model discussed in this paragraph, the trivalent iron would be the electron trap and the divalent nickel would be the hole trap. However, the decay of the nickel ESR signal at a lower temperature than the decay of Fe^{2+} ions suggests that there might be other ions involved in this process which can not be detected by ESR or optical spectrometers.

Another possible explanation of the room-temperature irradiation effects in the undoped samples is the formation of Ni^{+} ions after a room-temperature irradiation. This

would be the case if the ionizing radiation produced holes that became trapped on other defects or impurities in the crystal and which are not detectable by ESR. The corresponding electrons produced by the radiation would migrate along the c axis until they become trapped on Ni^{2+} or Fe^{3+} ions. Thus, in this latter model both nickel and iron act as electron traps.

Reduction Followed by Bleaching at 77 K

Another method of defect production in $LiNbO_3$, other than irradiation of undoped samples, is reduction at high temperature. Sequential reducing treatments involve heating the sample above room temperature while keeping it surrounded by an atmosphere with a low oxygen partial pressure, such as argon. Figure 10 shows the results of such a sequential reduction. In this case, the sample was was held at an elevated temperature in an argon atmosphere for one-hour periods of time and then cooled down to allow the defect concentrations to be monitored. This step reduction procedure was continued up to 650°C in steps of 50°C.

Traces of impurities, such as transition-metal ions, are present in lithium niobate in the parts-per-million concentration range. As $LiNbO_3$ crystals are reduced, some of these impurity ions change valence state. These changes in valence state can be monitored by ESR. After each complete cycle in our reduction procedure, the sample was cooled to 77 K. These reduction treatments decreased or, for redu-

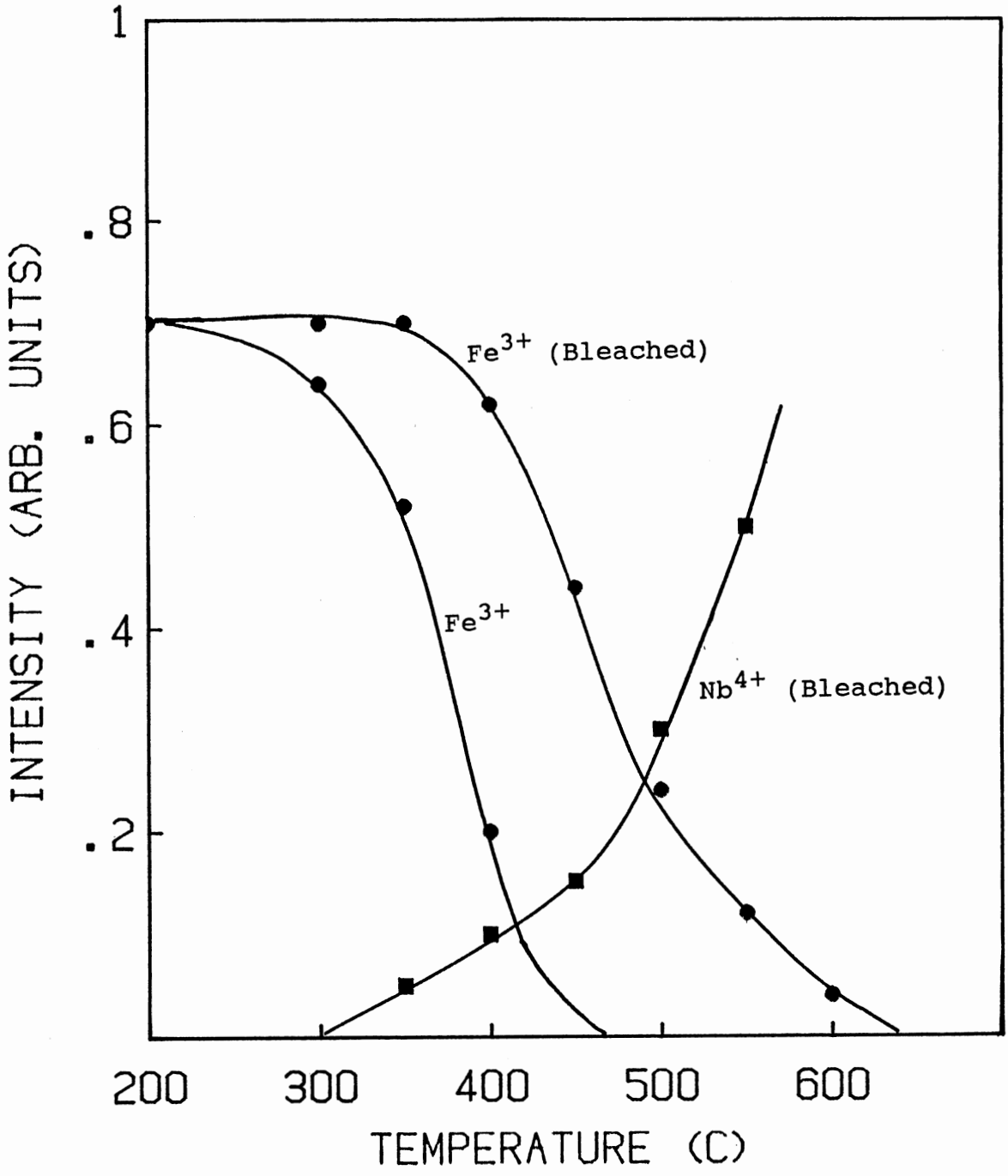

Figure 10. Results of 77-K optical bleaching of reduced $LiNbO_3$.

cing temperatures above approximately 450°C, completely eliminated the Fe^{3+} ions. When the reduction treatment was done at temperatures between 200°C and 600°C, subsequent exposure to visible and UV light from an unfiltered 150-W xenon lamp resulted in recovery of the Fe^{3+} ESR signal. These results are shown in figure 10. However, this recovery of the Fe^{3+} ESR signal does not occur in samples that are reduced at higher temperatures. After reducing at 650°C, no Fe^{3+} ESR signal can be recovered. The optical bleaching at 77 K with the unfiltered lamp also introduces a Nb^{4+} ESR spectrum in reduced $LiNbO_3$ samples. Figure 10 shows the intensity of the Nb^{4+} ions after bleaching. As the reducing temperature is increased, the optical bleaching produces a more intense Nb^{4+} ESR spectrum. This agrees with the previous work of Ketchum et al. [39].

As an explanation of the experimental data presented in the preceding paragraph, we propose that in the initial stages of the reduction process we are only producing Fe^{2+} ions as the responsible defect which will act as an electron source. Then during the subsequent optical bleaching at 77 K, the electrons from Fe^{2+} ions are excited into the conduction band by absorbing a visible photon. These electrons would drift or diffuse until trapped on Nb^{5+} ions to form paramagnetic Nb^{4+} ions.

$$Fe^{2+} + h\nu \longrightarrow Fe^{3+} + e^{-}$$

$$Nb^{5+} + e^{-} \longrightarrow Nb^{4+}$$

In the process described above, the bleaching light restores

the reduced Fe^{2+} ions back to their original charge state of Fe^{3+} ions.

Reducing the $LiNbO_3$ crystals at higher temperatures (greater than 600°C) converts all of the Fe^{3+} ions into the divalent state and also produces oxygen vacancies [40-44]. These latter defects are often referred to as F centers in analogy with the anion vacancy centers in alkali halides and simple oxides. The production of these vacancies is accompanied by the appearance of a broad optical absorption band peaking at 500 nm. This band was initially observed in the early 1970s [27,38] and was studied in more detail in the early 1980s [43,44]. We believe that this production of F centers inhibits the ability of the 77-K optical bleach to change the charge state of iron. This can be explained by considering the effect of the 77-K bleaching on F centers. The F centers can be converted into F^+ centers by optical bleaching at 77 K as shown by Sweeney and Halliburton [43]. The F centers would be the new electron source during the 77-K bleaching and thus some of the released electrons would recombine with Fe^{3+} ions and change them back to the divalent state.

$$\text{F center} + h\nu \longrightarrow F^+ \text{ center} + e^-$$

$$Fe^{3+} + e^- \longrightarrow Fe^{2+}$$

In the suggested model discussed above, the presence of an optical absorption band peaking at about 760 nm after the 77-K optical bleach is attributed to the formation of F^+ centers [43]. Although the F^+ center is paramagnetic, there

has been no ESR signal observed by us or reported by others for it. This could be a result of extreme line broadening due to a fast spin lattice relaxation and multiple hyperfine interactions.

Characterization of Iron in $LiNbO_3$:Mg,Fe

The presence of magnesium in $LiNbO_3$ at doping levels greater than approximately 4.5 atomic percent has a major effect on the electron spin resonance spectrum of Fe^{3+} ions. Figure 11 shows the X-band ESR spectra of two $LiNbO_3$ crystals that had been co-doped with magnesium and iron. The magnesium level was 5% in both samples while the iron level was 100 ppm in one sample (trace a) and 200 ppm in the other sample (trace b). Both traces in figure 11 were taken at 77 K with the magnetic field parallel to the c axis. The microwave frequency was 9.30 GHz and the static field was modulated at 100 kHz. The spectrometer's gain was the same for both traces. The intensities of all the lines representing Fe^{3+} ions in trace (b) of figure 11 are twice the intensities of those in trace (a). To make the comparison of the two traces in figure 11 valid, the sample sizes were both chosen with the same dimensions of 2.4 x 2.4 x 10 mm^3.

The spectrum of Fe^{3+} ions (S = 5/2) in $LiNbO_3$ is extremely complicated when observed at 9.30 GHz (X band). The reason for these complications is the large magnitudes of the crystal field terms in the spin Hamiltonian for the Fe^{3+} ions. These terms are comparable to or larger than the

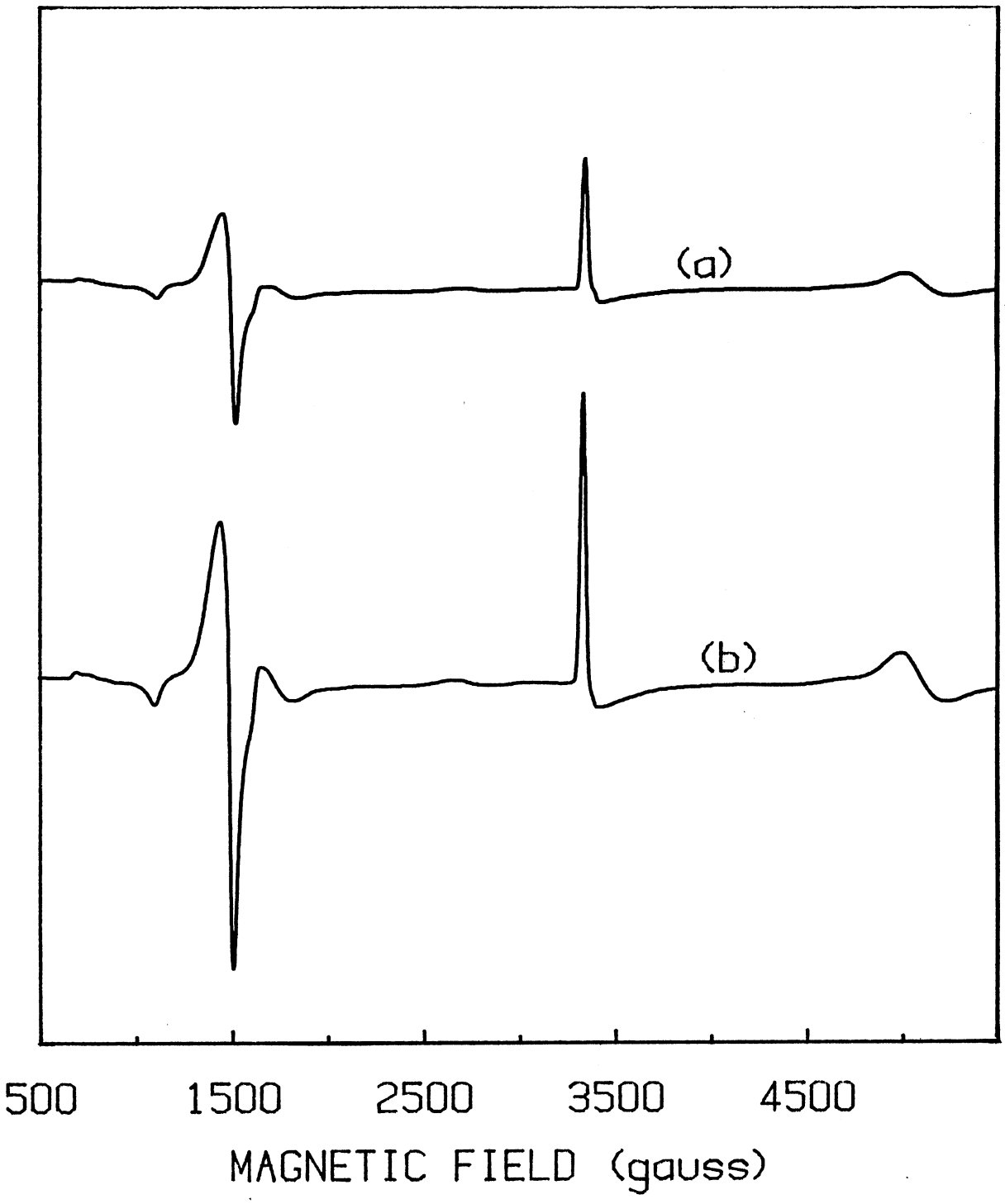

Figure 11. X-band ESR spectrum of $LiNbO_3$ doped with 5% Mg and either (a) 100 ppm Fe or (b) 200 ppm Fe.

electron Zeeman term, and this results in observable transitions that are normally "forbidden". To avoid these complications, a Ka-band ESR spectrometer was employed to provide a less complicated spectrum from the Fe^{3+} ions in the $LiNbO_3$:Mg,Fe samples. The Ka-band ESR spectra of $LiNbO_3$ samples that were (a) undoped and (b) 5% Mg and 200 ppm iron doped are shown in figure 12. To facilitate comparison, the samples used for figure 12 were the same size and the spectrometer's microwave power and modulation amplitude were kept constant. Each trace was taken at room temperature with the magnetic field parallel to the c axis. However, because of a different concentration of impurity ions in the two samples, the spectrometer's gain had to be different. The spectrometer's gain for trace (a) was 3 times larger than the gain setting for trace (b). Also, the spectrometer's gain for ESR transition at about 12.5 kG in trace (b) had to be reduced 10 times. The microwave frequency was 35.06 GHz and a 100 kHz static field modulation was used.

The spectrum from the undoped sample of $LiNbO_3$, trace (a) of figure 12, has previously been attributed to Fe^{3+} ions [30] in axially symmetric sites with the symmetry axis parallel to the crystallographic c axis. This spectrum contains five lines because Fe^{3+} has S = 5/2. The dashed portions (17.5-25 kG) in the traces in figure 12 were not actually recorded due to the maximum field limitations of the magnet.

The ESR spectrum from the co-doped $LiNbO_3$ sample, shown

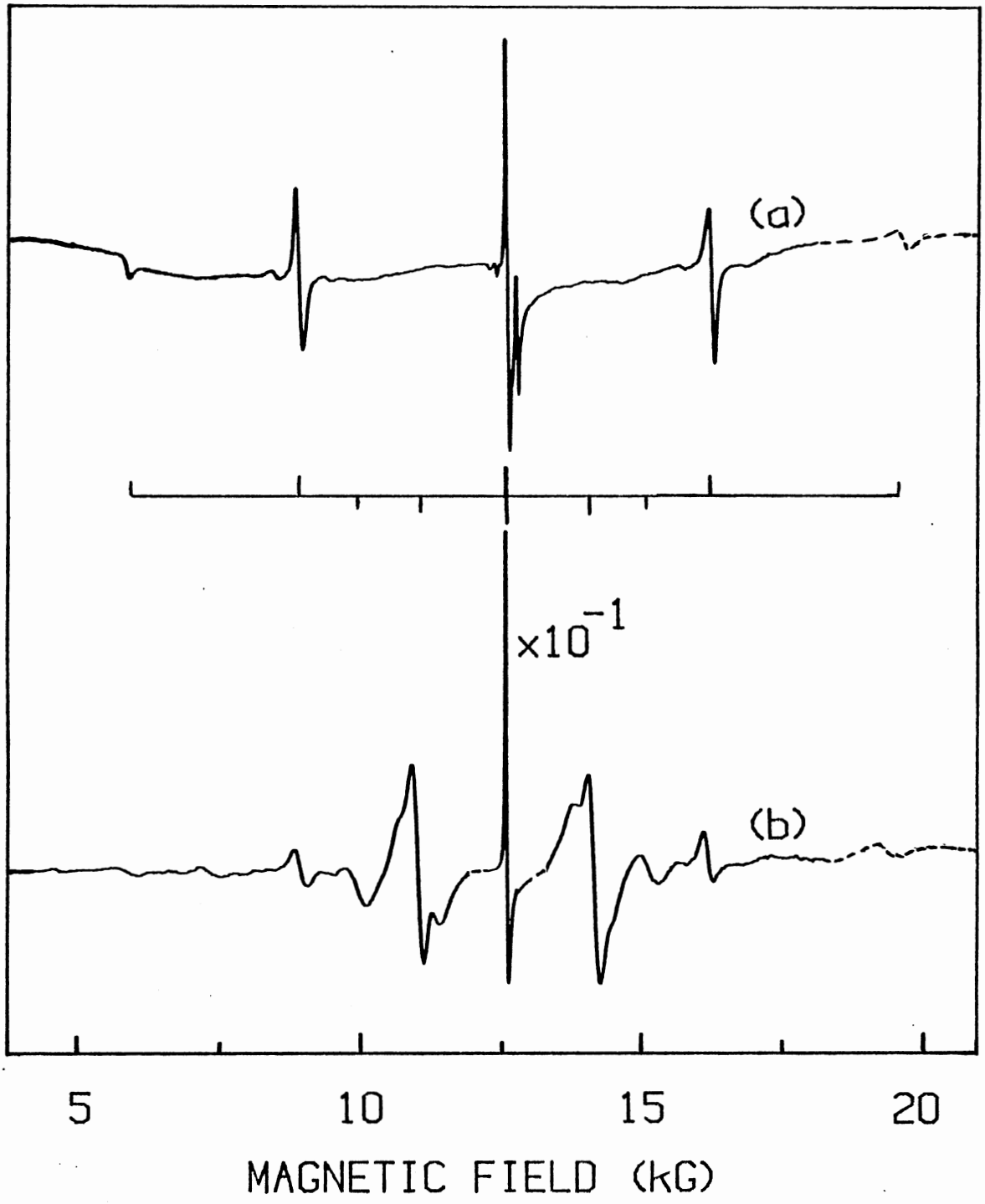

Figure 12. Ka-band ESR spectrum of $LiNbO_3$ either (a) undoped or (b) doped with 5% Mg and 200 ppm Fe.

in trace (b) of figure 12, has two primary sets of lines. One is the set of five lines corresponding to Fe^{3+} ions in the same environment as found in the undoped samples. The other is a second set of five lines corresponding to Fe^{3+} ions in a different environment. The intensity ratio of the two sets of lines suggests that the majority of Fe^{3+} ions end up in an environment different from that of undoped samples.

Lithium niobate can easily be reduced by heating to a high temperature in an argon atmosphere. As stated earlier, a primary result of this reducing process is the introduction of oxygen vacancies into the $LiNbO_3$ crystals. Reducing an undoped $LiNbO_3$ crystal results in the formation of an intense 500-nm optical absorption band. Subsequent optical bleaching at 77 K causes this 500-nm band to decrease substantially and a 760-nm band to appear [43]. This general behavior for undoped $LiNbO_3$ has been reported before [23,39]. Significantly different behavior is observed in a 5%-Mg-doped $LiNbO_3$ crystal [45]. The optical absorption spectrum obtained after reducing a $LiNbO_3$ crystal grown from a melt doped with 4.5% or more of magnesium contains a broad absorption band which can be separated into two overlapping bands, one peaking near 1200 nm and the other near 760 nm [45]. In contrast to reduced undoped samples of $LiNbO_3$, the subsequent optical bleaching at 77 K after reduction does not change the optical absorption spectrum of these highly doped samples.

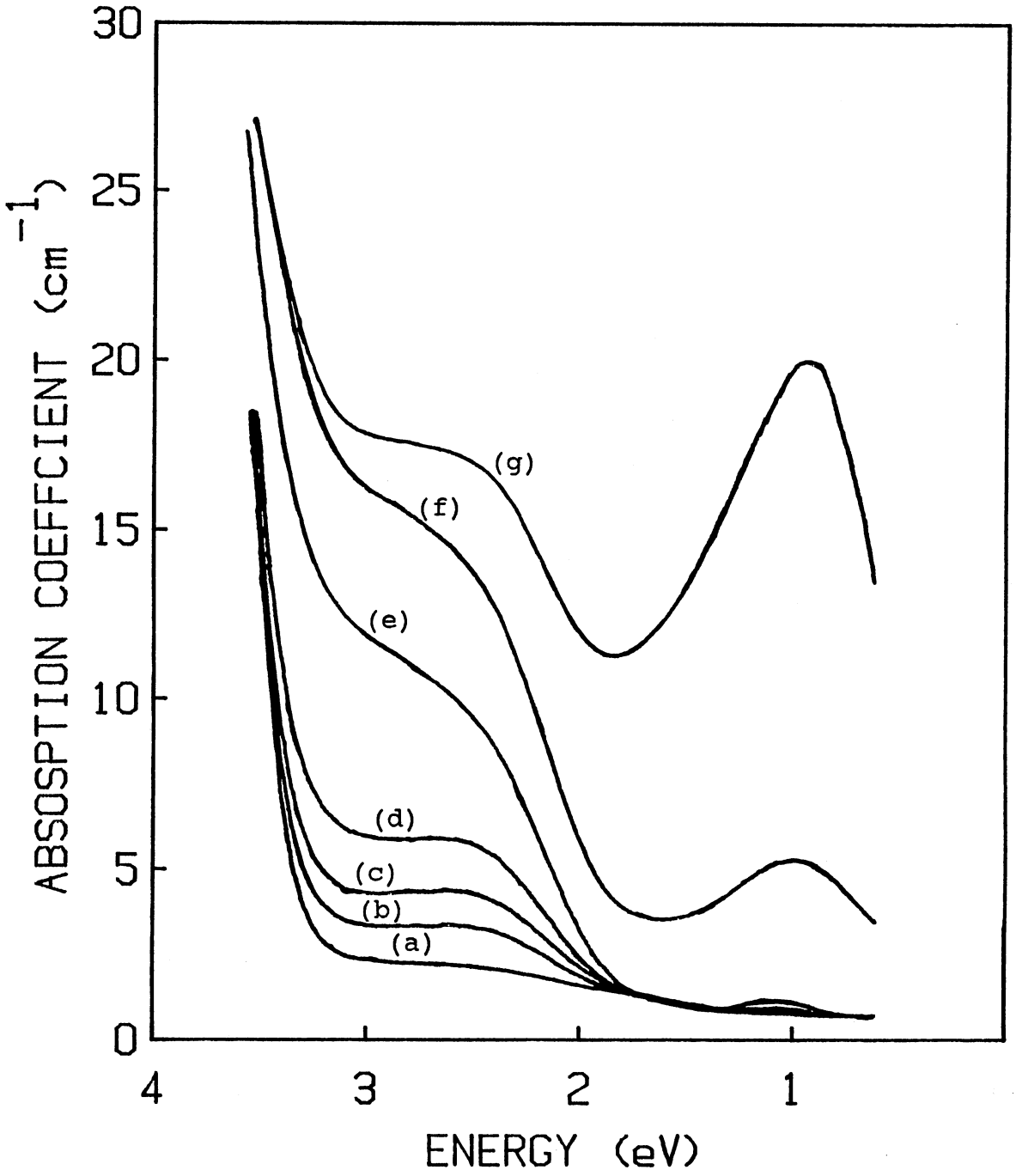

Figure 13. Optical absorption of $LiNbO_3$:Mg,Fe after a series of reductions at (a) before, (b) 500°C, (c) 600°C, d) 700°C, and (e) 800°C.

Optical absorption spectra of a $LiNbO_3$ crystal co-doped with iron and magnesium after a series of argon reductions are shown in figure 13. All of these optical absorption spectra were taken at room temperature. Unlike the undoped $LiNbO_3$ crystals, the optical bleaching at 77 K does not effect the optical absorption spectrum of reduced $LiNbO_3$ samples co-doped with magnesium and iron. This agrees with the previous work of Sweeney et al. [45] on the $LiNbO_3$ crystals that had been doped with only the magnesium.

To find correlations between the point defects monitored with the ESR spectrometer and the defects represented by the reduction-induced optical absorption bands, optical and ESR samples were cut from the same boule of $LiNbO_3$ and were reduced under exactly the same experimental conditions. The ESR sample was rectangular in shape, approximately 2 x 3 x 8 mm^3 with the c axis being along the smallest dimension. The optical samples were approximately 2 x 10 x 15 mm^3 plates, oriented such that the c axis was perpendicular to the plane of the plate.

Valence changes of impurity ions can be monitored by ESR. In figure 14, we show the behavior of a series of defects as a function of the reducing temperature for a $LiNbO_3$:Mg,Fe sample. Included in the figure are the intensity of Fe^{3+} ions as monitored with the ESR spectrometer, the growth of two optical bands at 460 and 1300 nm, and the decay of OH^- molecular ions as measured by the infrared spectrophotometer. This reducing experiment was carried out

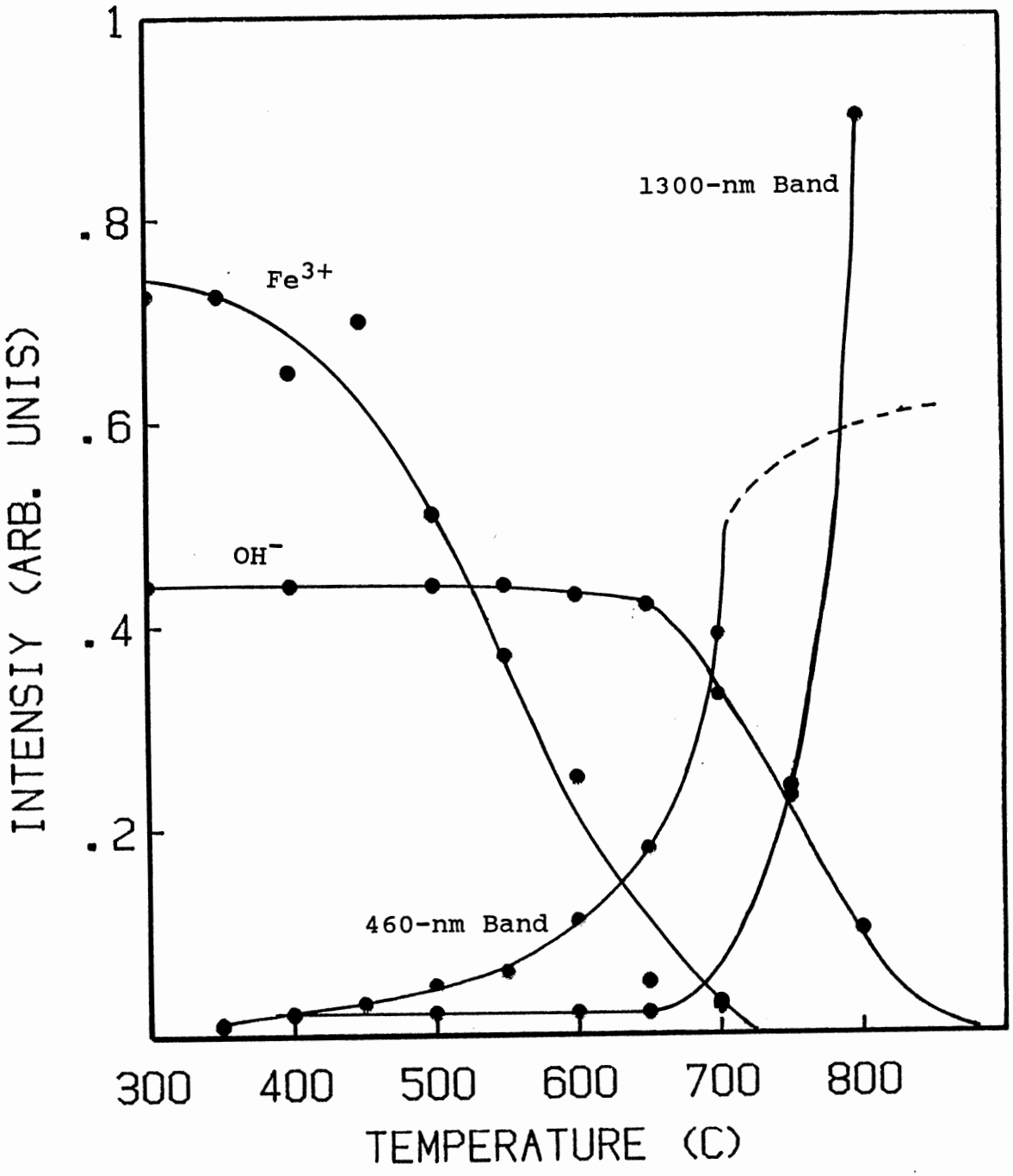

Figure 14. Results of reducing a $LiNbO_3$:Mg,Fe crystal.

by sequentially heating the sample in an argon atmosphere in steps of 50°C. The samples were kept at the elevated temperature for one hour and then cooled for measurements. This procedure was repeated up to 800°C. The intensity of the Fe^{3+} ESR spectrum was measured at 77 K after each step. The visible and infrared absorption measurements were carried out at room temperature.

The presence of the magnesium ions in the $LiNbO_3$ crystals affects the OH^- absorption band that is monitored with an infrared absorption spectrophotometer. The OH^- absorption band peaks at 2.87 μm in undoped samples of $LiNbO_3$. The OH^- absorption band in samples doped with 5% or more of magnesium peaks at 2.83 μm [26].

The intensity of the optical absorption bands shown in figure 13 are plotted in figure 14 as a function of the reducing temperature. The rapid growth of the 1300-nm band above 700°C causes it to significantly perturb the 460-nm band. Because of this overlap it is very difficult to accurately determine the intensity of the 460-nm band above 700°C. The anti-correlation between the drop of the Fe^{3+} ESR spectrum and the increase of the optical absorption band at 460 nm suggests that this band be assigned to Fe^{2+} ions.

The 1300-nm band in figure 13 could be the overlap of two or more bands. As suggested previously by Sweeney et al. [45], reduction of a 5% Mg-doped crystal in vacuum at 1000°C for 1 hour produces a broad band near 1200 nm with a shoulder in the 500-800 nm region. Those investigators

suggested that the broad band near 1200 nm could be decomposed into two bands. This spectral decomposition was done by subtracting the F^+ center optical absorption band (peaking near 750 nm) produced in an undoped sample of lithium niobate from the absorption band of the reduced 5% Mg-doped sample of $LiNbO_3$. The result of this subtraction was a sharp absorption band peaking near 1200 nm without any shoulder in the 500-800 nm region of the spectrum. Thus, they concluded that the broad absorption band in reduced $LiNbO_3$:Mg is the overlap of two bands at 750 and 1200 nm. In our present case the overlap of 1200 and 750 nm band could not result in a 1300 nm band in a reduced $LiNbO_3$:Mg,Fe, however, because of the rapid growth of the 460 nm optical absorption band due to Fe^{2+} ions and its strong overlap with 1300-nm band it is difficult to justify a shoulder on 1300-nm band. Thus, it is possible that the absorption band in $LiNbO_3$:Mg,Fe peaking near 1300 nm is an overlap of bands from three different defect centers, the F^+ center, the Mg-complex, and the Fe^{2+} ions. The decay of the OH^- absorption band at 2.83 μm as monitored by the infrared spectrophotometer correlates with the growth of the 1300-nm optical absorption band as shown in figure 14.

Characterization of Titanium in $LiNbO_3$

The behavior of titanium in $LiNbO_3$ is investigated and characterized by ESR and optical absorption techniques. The Ti-doped samples were studied after 77-K irradiations and

after a series of reduction treatments. The effect of a 77-K optical bleach after irradiation was also investigated.

77-K Irradiation

An electron spin resonance spectrum taken from an as-grown $LiNbO_3$ crystal doped with 1% TiO_2 in the melt is shown in figure 15 (a). Subjecting such a crystal to ionizing radiation at 77 K produces two distinct ESR spectra, as shown in figure 15 (b). One is a holelike resonance at g_c = 2.025 and the other is an electronlike signal at g_c = 1.962. Both traces in figure 15 were taken at 30 K, and the microwave frequency was 9.42 GHz. The static field modulation was 12.5 kHz and the magnetic field was perpendicular to the c axis of the crystal. The total dose received by this sample was approximately 1 Mrad (si) during the irradiation at 77 K. The holelike signal is similar to that previously reported by Schirmer and Von der Linde [46] in undoped lithium niobate after a 77 K irradiation. These investigators attributed this holelike ESR spectrum to O^- ions. The Nb^{4+} ESR spectrum that is usually observed in undoped $LiNbO_3$ samples after a 77 K irradiation was absent in this Ti-doped sample. The Nb^{4+} ion has been suggested to be an electron trap [46]. The other dominant line in figure 15 (b) with a field value of 3647 G has been previously assigned to Ti^{3+} ions by Juppe and Schirmer [47].

An optical absorption spectrum taken at 80 K from an as-grown Ti-doped $LiNbO_3$ crystal is shown in figure 16 (a). This crystal is nearly transparent throughout the visible

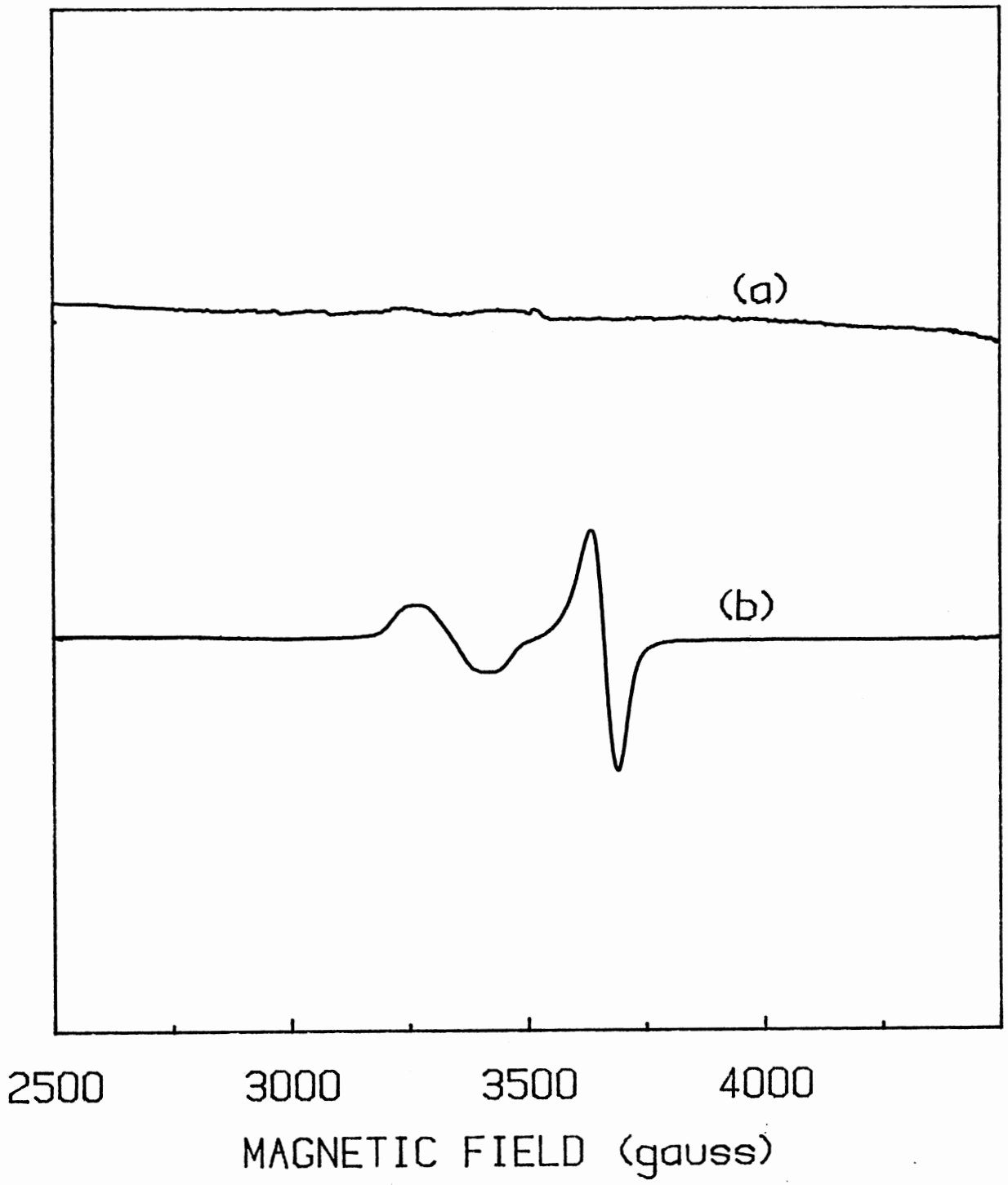

Figure 15. 30-K ESR spectrum of $LiNbO_3$:Ti (a) before and (b) after irradiation at 77 K.

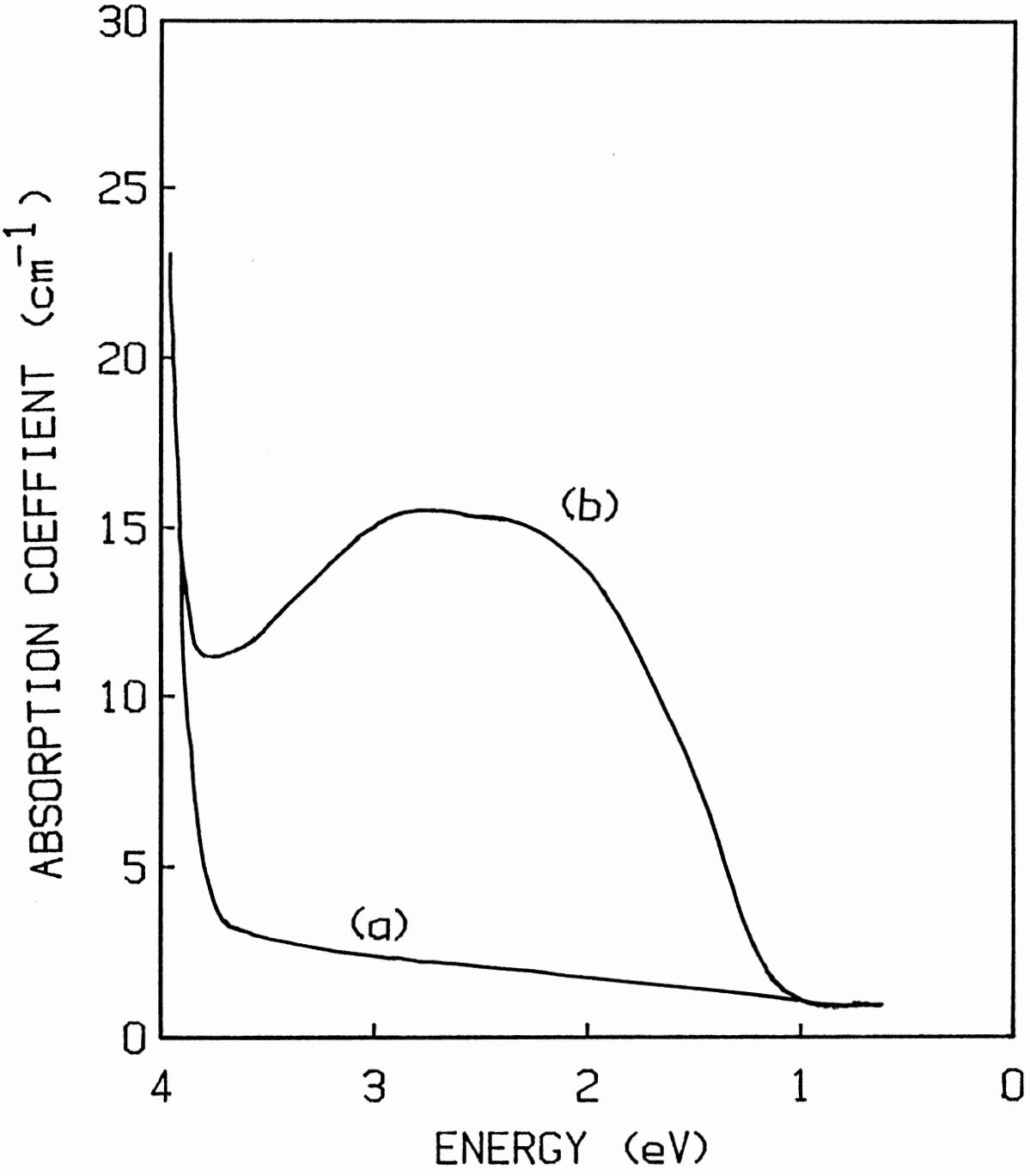

Figure 16. Optical absorption of $LiNbO_3$:Ti (a) before and (b) after an electron irradiation at 85 K.

spectrum. Below the band edge, beginning about 300 nm, there is essentially zero absorption in the near ultraviolet through the visible region and into the infrared prior to either radiation or reduction. Figure 16 (b) shows the optical absorption spectrum after an irradiation at approximately 85 K. Two overlapping bands emerge in the visible region. The correlation in $LiNbO_3$:Ti samples between the radiation-induced optical absorption spectrum shown in figure 16 (b) and the ESR spectrum shown in figure 15 (b) is established by a pulsed thermal anneal. The pulsed thermal anneal procedure consisted of first irradiating the sample near liquid nitrogen temperature and then heating the sample in steps of 20°C with a five-minute holding time at each temperature. The sample was immediately cooled down after each anneal step for measurement. The results of the pulsed thermal anneal are shown in figure 17 as a plot of the intensities of the ESR spectrum of the Ti^{3+} ions and the optical absorption band at 510 nm as a function of temperature from 80 K to 300 K. The ESR spectrum and the optical band decay at nearly the same rate in the 100 K to 160 K region.

Reduction of Ti-doped $LiNbO_3$

We assume that titanium enters the $LiNbO_3$ lattice as Ti^{4+} ions. Reduction of the lithium niobate results in a conversion of these Ti^{4+} ions to Ti^{3+} ions. Juppe and Schirmer [47] described the Ti^{3+} ESR spectrum in $LiNbO_3$ for the first time. They observed the Ti^{3+} ions in a Ti-diffused lithium niobate substrate annealed at 900°C in an

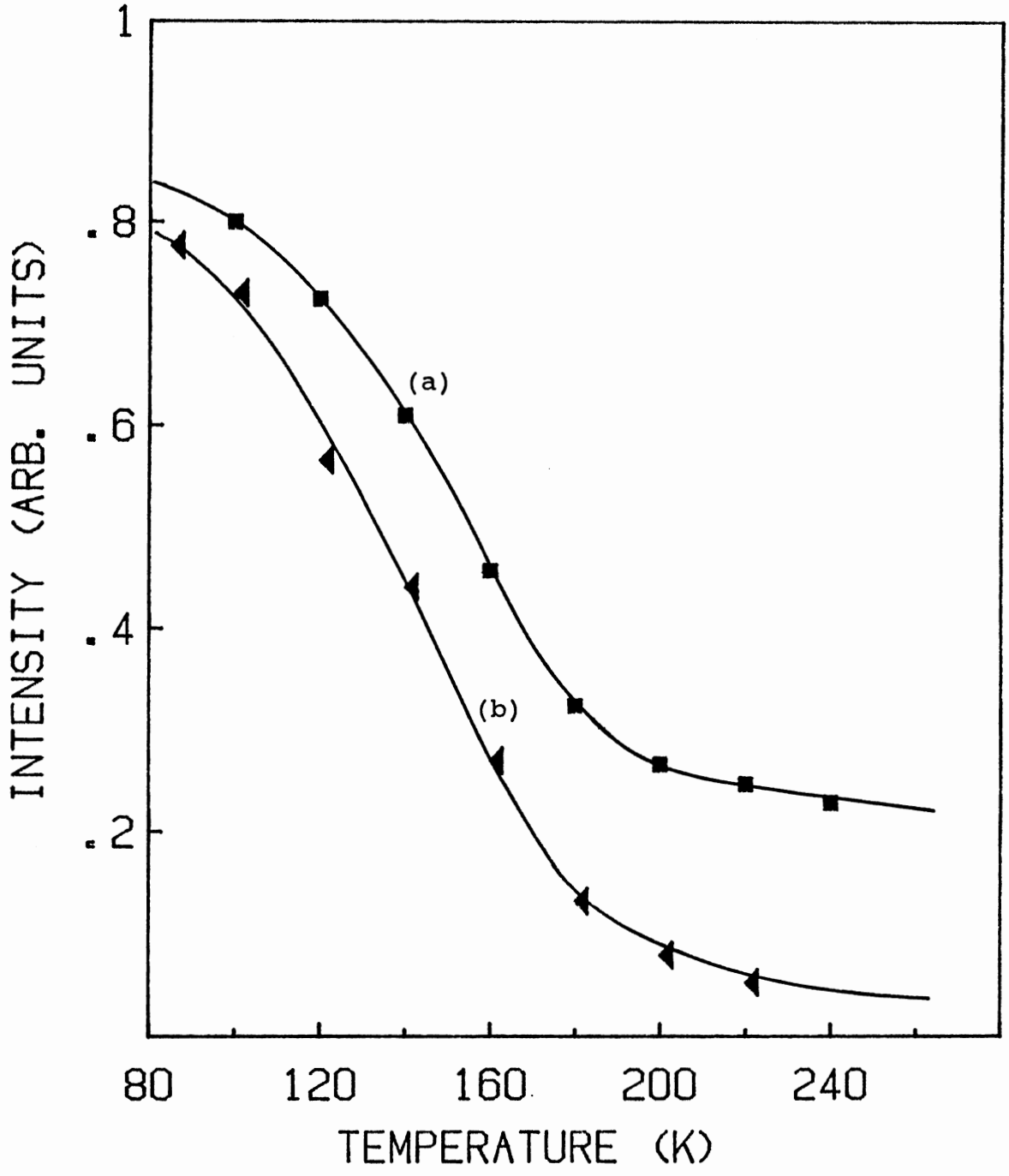

Figure 17. Pulsed thermal anneal of an irradiated $LiNbO_3$:Ti crystal, (a) optical absorption band and (b) Ti^{3+} ESR spectrum.

H_2 atmosphere for 1/2 hour.

Figure 18 shows the ESR spectra of the Ti^{3+} ions in a $LiNbO_3$:Ti crystal. The sample had been reduced in an argon atmosphere at 800°C for 1 hour. Trace (a) in figure 18 was taken at 77 K with the magnetic field parallel to the c axis while trace (b) was taken with the magnetic field perpendicular to the c axis.

The optical absorption spectrum of Ti^{3+} ions in $LiNbO_3$ is shown for the first time in figure 19. Reduction of $LiNbO_3$:Ti crystals at 800°C results in two strongly overlapping optical absorption bands. One of the bands peaks at about 660 nm and the other peaks near 450 nm. The correlation of the ESR spectrum and the optical absorption bands was investigated by reducing two samples under the same experimental conditions. A sequential reduction was carried out by heating the samples in a stainless steel tube in an argon atmosphere. The steps were 100°C with 1 hour duration for each annealing step. The results of this step annealing are shown in figure 20.

ENDOR Results

Electron-nuclear double resonance (ENDOR) experiments have been performed on a number of lithium niobate samples. This type of experiment consists of monitoring the intensity of an ESR signal from a paramagnetic center under conditions of saturating, or partially saturating, microwave power while simultaneously sweeping an rf frequency over a wide

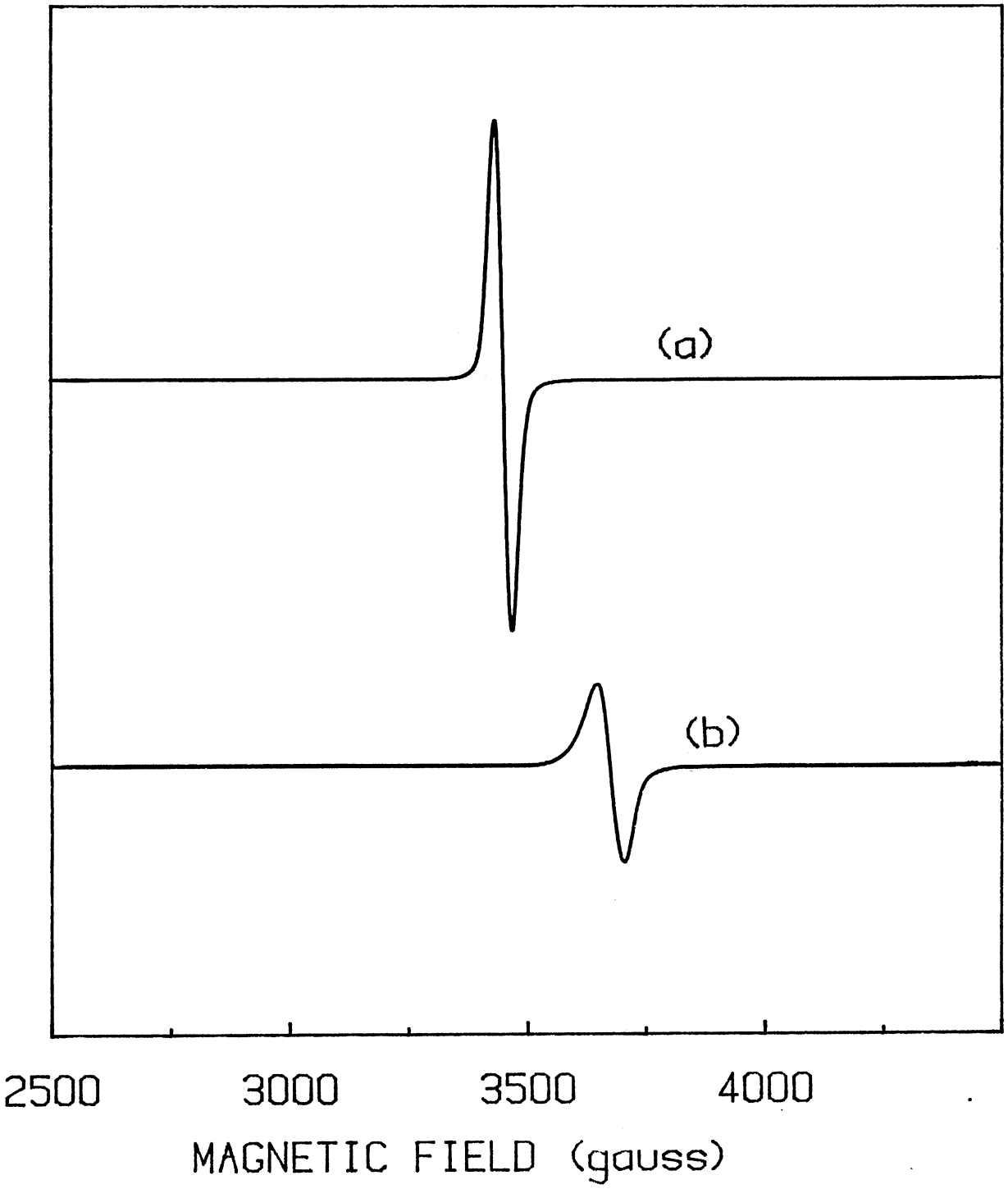

Figure 18. ESR spectrum of $LiNbO_3$:Ti after an 800°C argon reduction, (a) magnetic field parallel to the c axis and (b) perpendicular to the c axis.

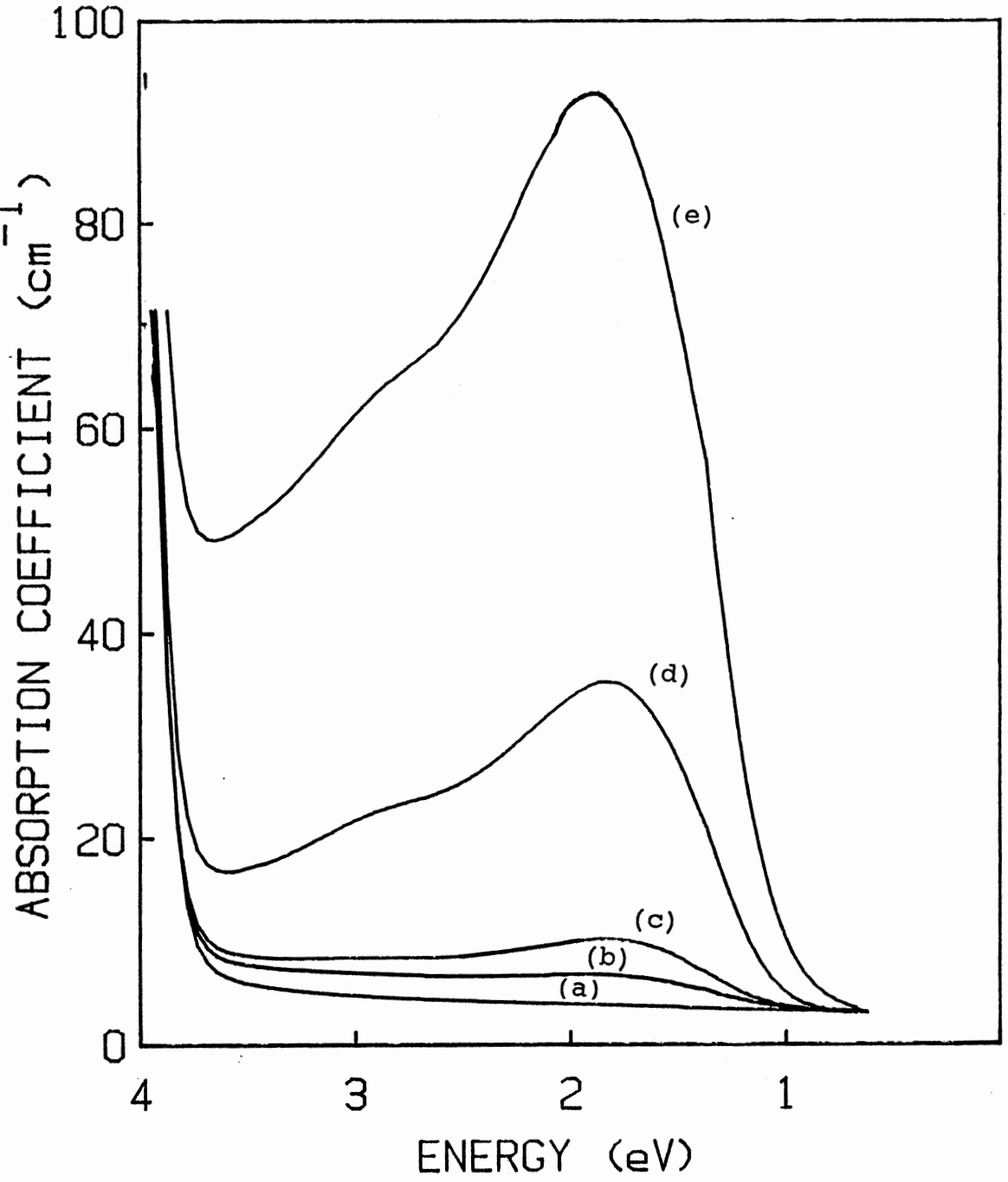

Figure 19. Optical absorption spectrum of $LiNbO_3$:Ti after a series of argon reductions, (a) before, (b) at 500°C, (c) at 600°C, (d) at 700°C, and (e) at 800°C.

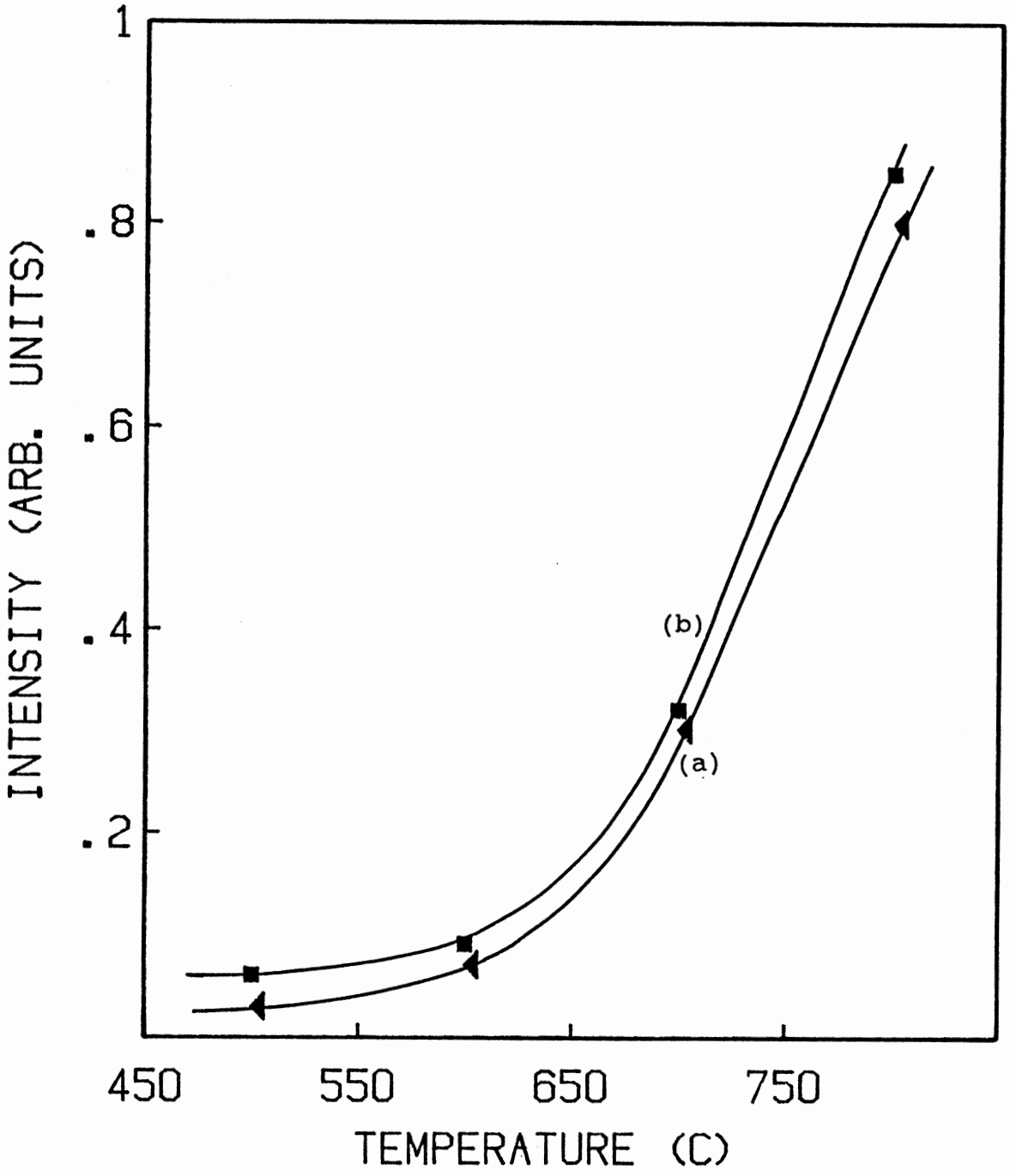

Figure 20. Results of reducing a $LiNbO_3$:Ti crystal at progressively higher temperatures, (a) Ti^{3+} ESR spectrum and (b) optical absorption band.

frequency range, typically 1-100 MHz. The resulting absorption of rf power by different nuclear species (when their resonance condition is met) provides the ENDOR signal. The spin flips of the nuclear species is detected via the change in the intensity of the monitored ESR signal. In summary, we can say that ENDOR is a sophisticated spectroscopic technique in which the ESR intensity is monitored to detect nuclear magnetic resonance transitions. In principle, this is an easily done experiment, but in practice a significant change in the intensity of an ESR signal can take place only if the nuclear spin relaxation times and the rf pumping rates have the appropriate values. This will happen if the proper conditions such as temperature, microwave power, rf power, etc. are established.

Figure 21 shows the ENDOR spectrum of the radiation-induced trapped-hole center in an undoped sample of lithium niobate. The data were taken at 30 K after the trapped-hole center was produced by a 77 K x-irradiation. The magnetic field was parallel to the crystal's c axis. The rf frequency was swept from 1 to 10 MHz while being frequency modulated at 12.5 kHz with a modulation depth of 250 kHz. The dominant line observed in figure 21 is from the distant ^{7}Li nuclei (i.e., those ^{7}Li nuclei that are far removed from the immediate vicinity of the paramagnetic hole center). The derivative of this dominant absorption line is centered at 5.61 MHz. The other lines of less intensity in figure 21 have not been identified yet.

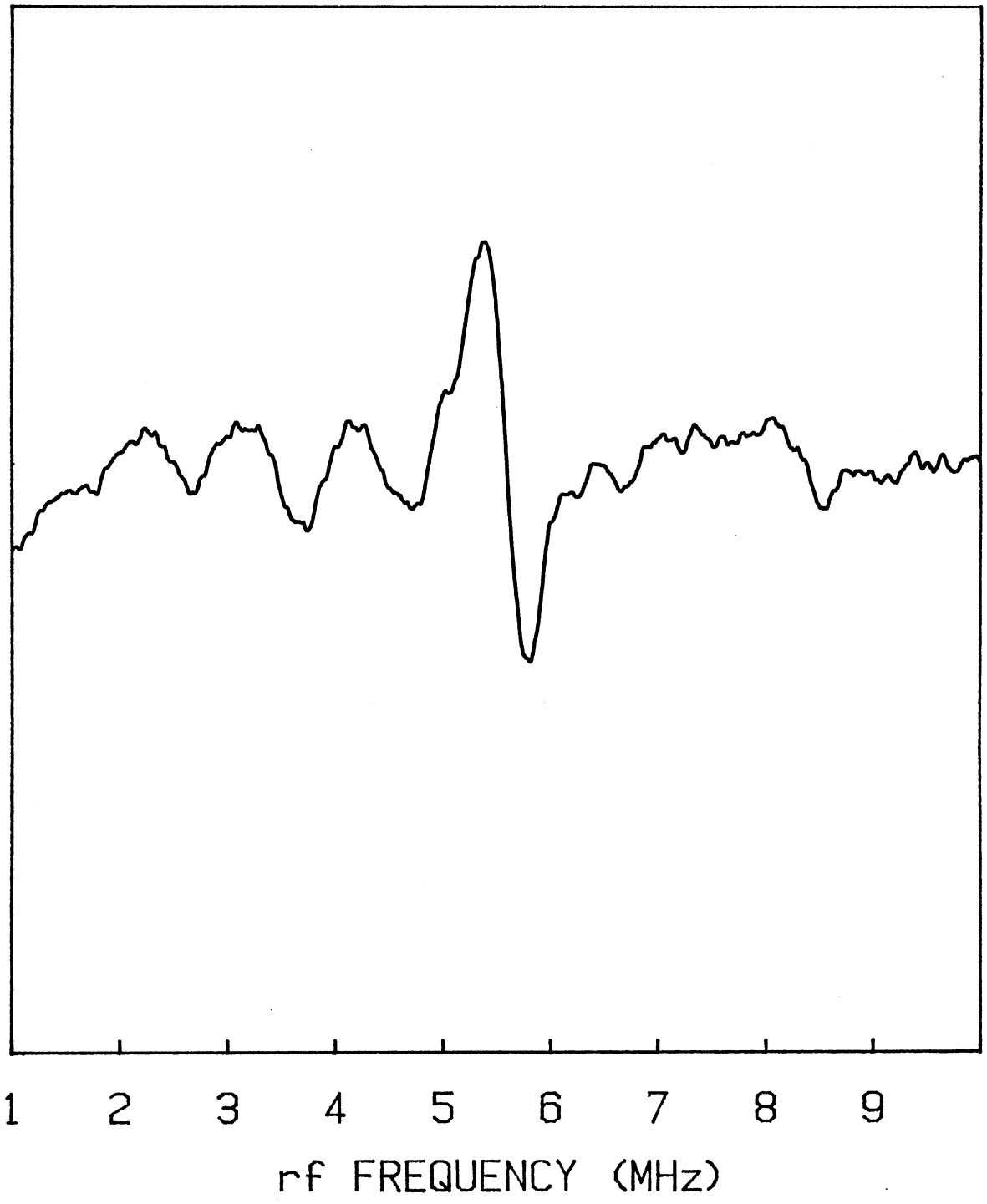

Figure 21. ENDOR spectrum of the trapped-hole center in $LiNbO_3$. Observed at 30 K with magnetic field parallel to the c axis.

Other ENDOR experiments were performed on samples of lithium niobate doped with 1% titanium (in the melt). The paramagnetic center investigated was the Ti^{3+} ion; in one case it was produced by ionizing radiation at 77 K and, in the other case, it was produced by a high-temperature reduction in an argon atmosphere.

The ENDOR spectrum obtained from Ti^{3+} ions after a 77-K irradiation is shown in figure 22. The $LiNbO_3$:Ti sample was x-irradiated in a styrofoam cup filled with liquid nitrogen and the sample received a total dose of approximately 1 Mrad (Si). The ENDOR results presented in figure 22 were taken at 13 K with the magnetic field parallel to the crystal's c axis. The microwave frequency was 9.44 GHz and the magnetic field position for the Ti^{3+} ESR line was approximately 3460.2 Gauss. The spectrometer's gain was 5×10^5 and the microwave power was approximately 6.3 mW (15 dB attenuation setting). The rf power was set for 1 dB attenuation (approximately 160 W) and the rf frequency was swept from 1 MHz to 26 MHz and was frequency-modulated at a rate of 12.5 kHz with 200 kHz modulation depth. The sweep time was 25 sec and the spectrometer's time constant was 100 ms. The spectrum reproduced in figure 22 is a computer accumulation of 10 consecutive sweeps.

The dominant line in the ENDOR spectrum shown in figure 22 is the line at about 5.7 MHz. An ENDOR angular dependence study of this spectrum does not show any change in the position of the line at 5.7 MHz whereas a strong angular

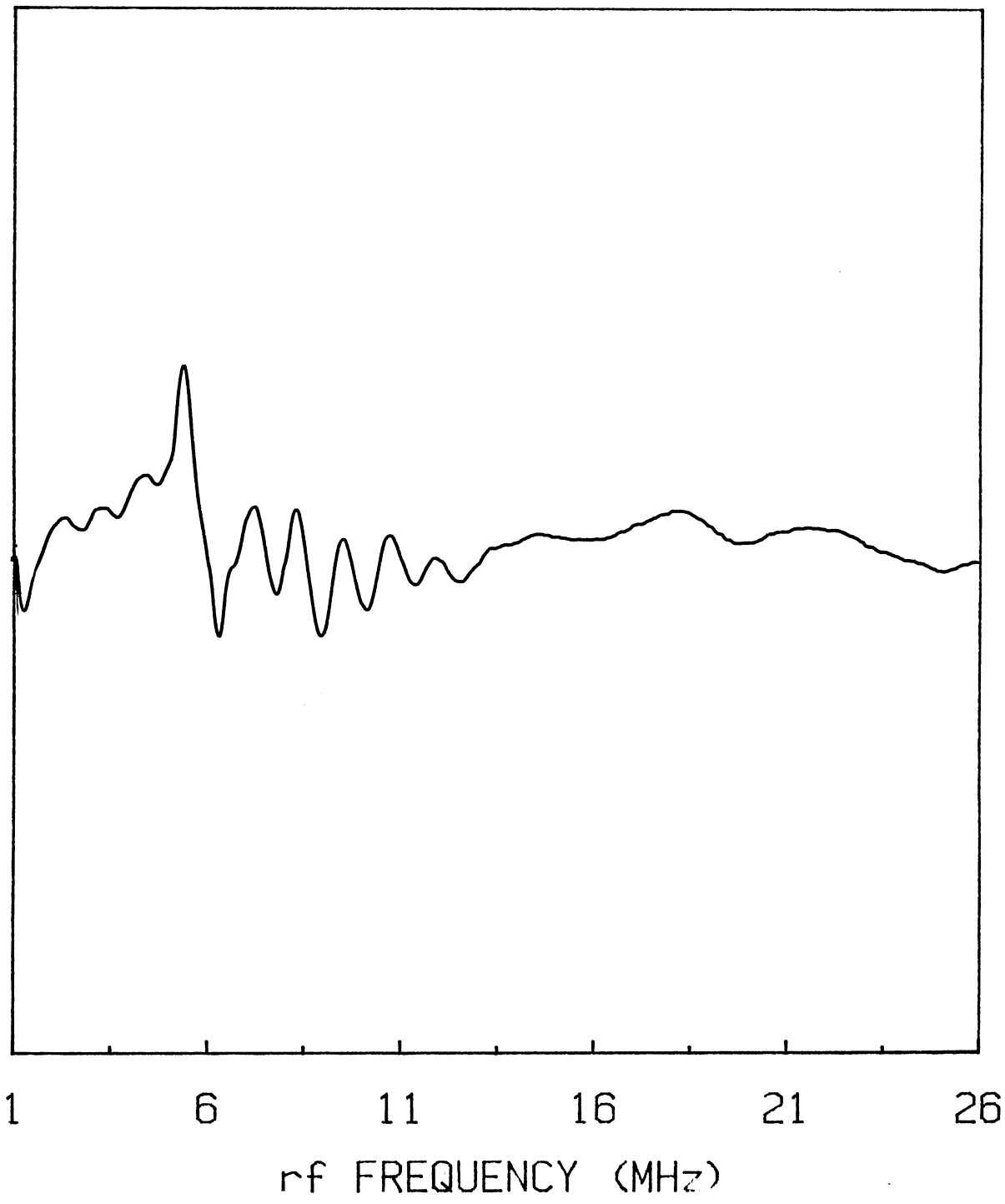

Figure 22. ENDOR spectrum of Ti^{3+} ions in $LiNbO_3$:Ti. Observed at 13 K after a 77-K irradiation. Magnetic field parallel to c axis.

dependence was observed for the other lines in the spectrum. This result suggests that the line at 5.7 MHz is a distant ENDOR line and its frequency matches the nuclear resonance frequency of free ^{7}Li nuclei. The other lines in the spectrum of figure 22 can be viewed as a set of 10 lines in the range from 1 to 13 MHz. This set of 10 lines have almost equal spacings of approximately 1 MHz. The linewidth of these ENDOR spectra lines are measured by estimating the rf range from the maximum peak of the derivative of the ENDOR absorption spectrum to the minimum peak of the derivative of the ENDOR spectrum. The linewidth measured in this 10 line spectra is in the order of 0.5 MHz.

To identify the responsible nuclei for the 10-line ENDOR spectrum observed, we consider two possibilities. The first choice is based on the assumption that only one nuclear species is responsible for the observed 10-line spectrum. The closest candidate would be an aluminum nucleus with I = 5/2 and 100% natural abundance. The defect complex formed by aluminum and titanium could be hypothesized as an Al^{3+} ion being one of the possible charge compensators for the existing lithium vacancies (about 4.5%) in the lattice. This Al^{3+} ion would be in an oxygen octahedron next to the oxygen octahedron occupied by the Ti^{4+} ion along the c axis. Thus, the oxygen octahedra along the c axis would be filled in the following sequence, lithium vacancy, a titanium ion (replacing a niobium ion), an aluminum ion (in an otherwise vacant oxygen octahedron), and a second lithium

vacancy.

Although, a nucleus with I = 5/2 could result in a maximum number of 10 lines provided that the strength of the nuclear electric quadrupole interaction is comparable to the nuclear Zeeman interaction in the ENDOR spin-Hamiltonian, but there are other aspects such as the magnitude of the hyperfine interaction, the natural abundance of the nuclear species, and the nuclear magnetic resonance frequency of the free nucleus which should be considered.

Another possibility which might explain the 10-line ENDOR spectrum in the irradiated $LiNbO_3$:Ti crystal is that more than one nuclei is involved. The analysis and identification of such a spectrum is very difficult. Furthermore, without a complete analysis of an ENDOR spin-Hamiltonian, it is impossible to find a definitive answer for the identity of the nuclei responsible for these ENDOR absorption lines.

The ENDOR spectrum from Ti^{3+} ions in $LiNbO_3$:Ti which have been produced by a high temperature reduction is shown in figure 23. This Ti-doped sample of lithium niobate was annealed to a temperature of 800^{o}C in an argon atmosphere for a duration of one hour. This procedure assured a large concentration of Ti^{3+} ions as a result of reducing the charge state of Ti ions from 4+ to 3+.

The spectrum in figure 23 was taken at 13 K and the magnetic field was parallel to the crystal's c axis. The rf frequency was swept from 1 to 26 MHz with a sweep time of 25 sec. The rf power was set at 1 dB attenuation (approxi-

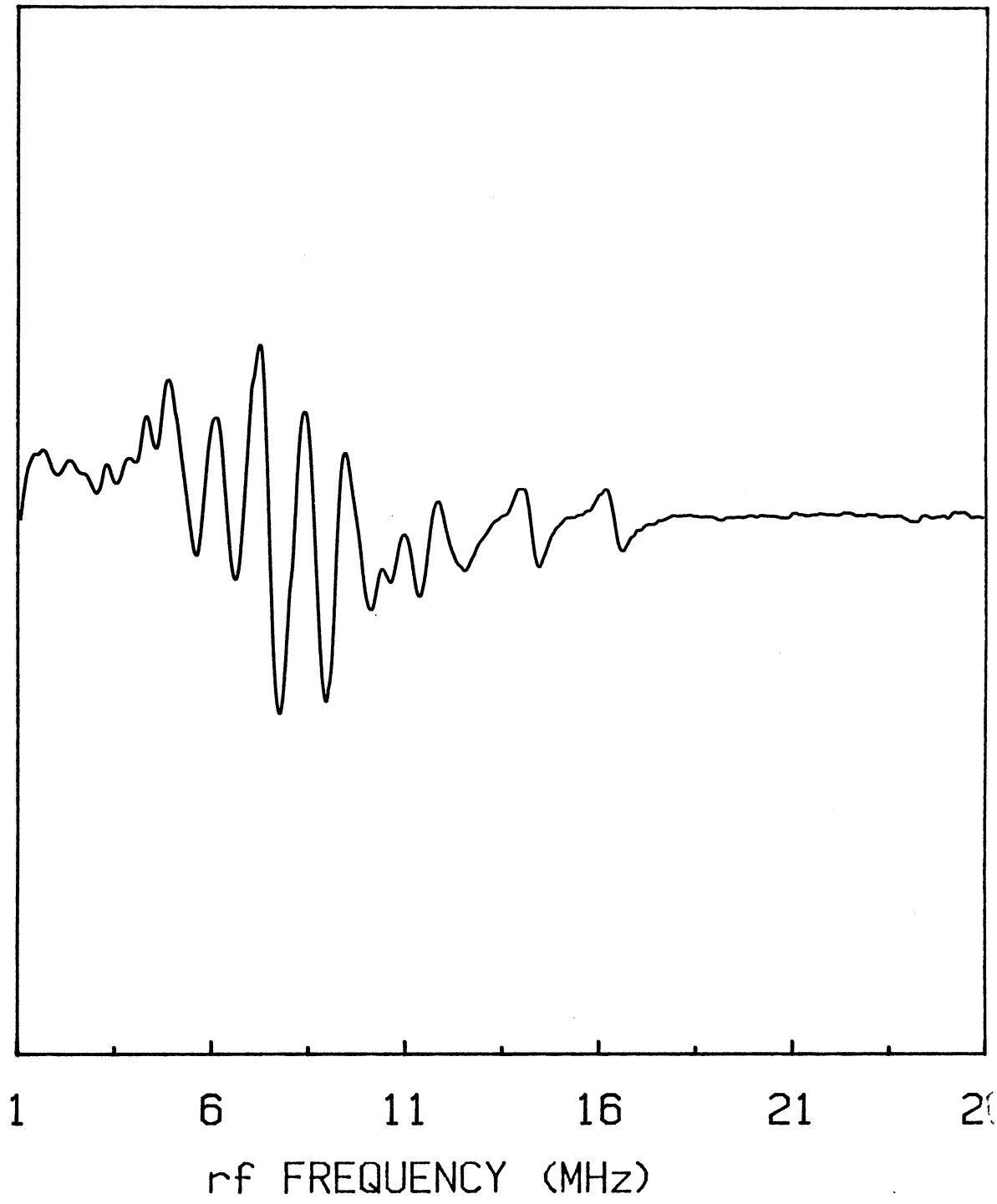

Figure 23. ENDOR spectrum of Ti^{3+} ions in $LiNbO_3$:Ti. Observed at 13 K after a high-temperature argon reduction. Magnetic field parallel to c axis.

matly 160 W) and the rf was frequency modulated at 12.5 kHz with a modulation depth of 200 kHz. The microwave frequency was 9.43 GHz and the microwave power attenuation was 15 dB (approximately 6.3 W). The spectrometer's gain was 2.5 x 10^5 with a time constant of 100 ms. The magnetic field for the ESR line of the Ti^{3+} signal was 3449.3 Gauss.

The trace shown in figure 23 consists of 18 lines in the range from 1 to 18 MHz. The line spacing of this spectrum is quite uneven and the line spacing seems to become larger at the high frequency end of the spectrum. A rough angular dependence study of this spectrum shows a tendency for the lines at the ends to move toward the center of the spectrum as the magnetic field is rotated away from the c axis.

The spectrum in figure 23 is extremely complex and will require a computer analysis of a complete ENDOR spin-Hamiltonian with subsequent simulations for some candidate nuclei. However, the linewidths and the spacings within the spectrum suggest that there may be more than one nuclei contributing to the observed spectrum. Furthermore, the observed spectrum in figure 23 can be separated into three regions. The first of these covers the range from 1 to 4.5 MHz, the second covers the range from 4.5 to 11 MHz, and the third covers the range from 11 to 17 MHz. Only the ENDOR lines in the middle region appear similar to those observed in the ENDOR spectrum from the Ti^{3+} ions produced by ionizing radiation and shown in figure 22. We assume that more

than one nuclei may be participating in the ENDOR spectrum from the Ti^{3+} ions produced by the high temperature reduction. A niobium nucleus with I = 9/2 could give rise up to 18 lines in principle. However, the line spacing and the spread of the absorption lines over the spectrum is quite complex and does not favor a choice of one nuclei such as ^{93}Nb responsible for the 18-line spectrum observed. Although an ENDOR spectrum from Ti nuclei is expected, however because of the low natural abundance of Ti nuclei, such spectrum has not been identified. It is possible that the ENDOR lines in the 1 to 4.5 MHz region of spectrum shown in figure 23 are from the Ti nuclei.

Figures 24 and 25 show the ENDOR spectra for the Ti^{3+} ions when the magnetic field is oriented perpendicular to the crystal's c axis. The results obtained from Ti^{3+} ions produced by a high-temperature reduction are presented in figure 24 while the results obtained from Ti^{3+} ions produced by ionizing radiation are shown in figure 25.

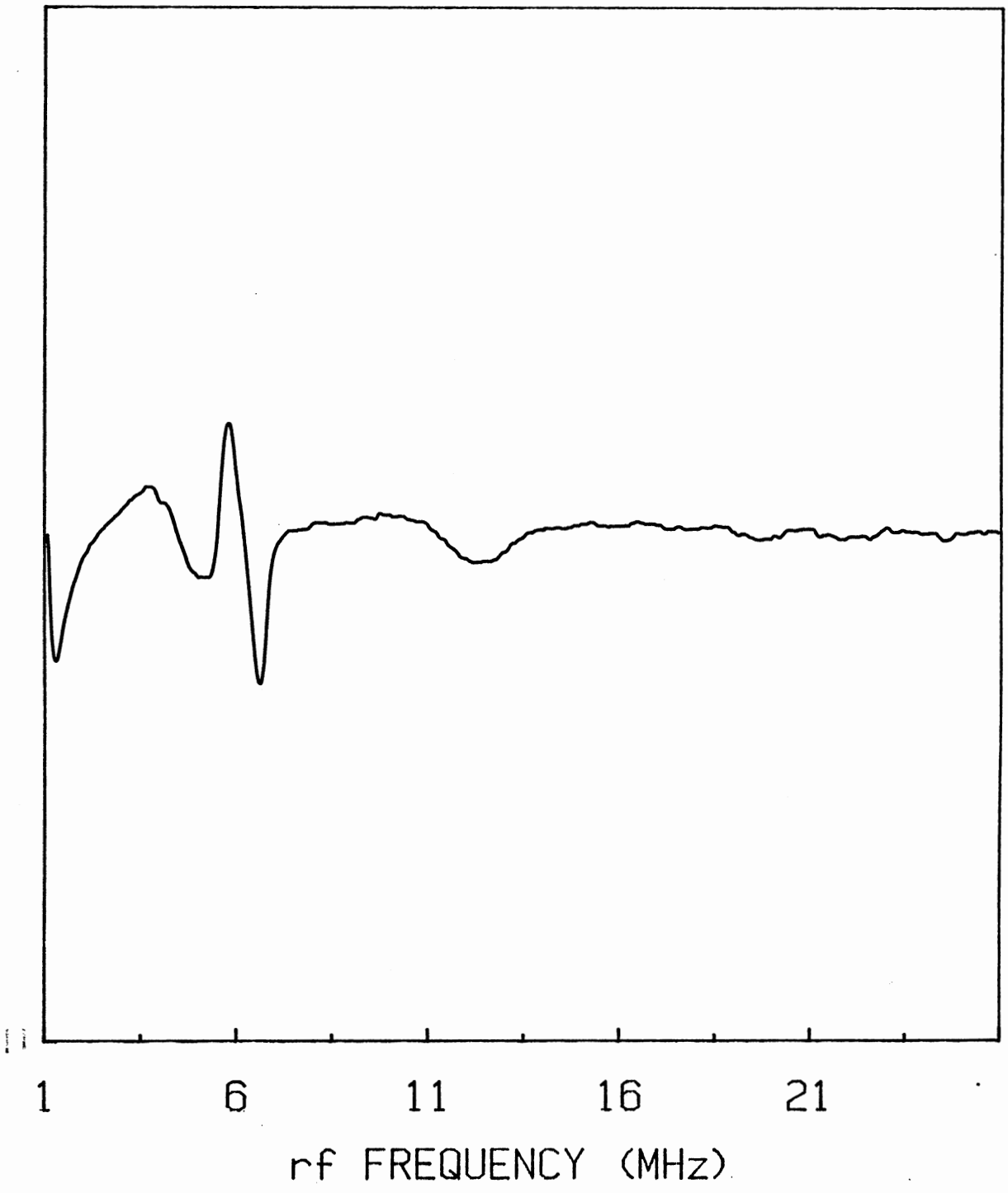

Figure 24. ENDOR spectrum of Ti^{3+} ions in $LiNbO_3$:Ti. Observed at 13 K after a 77-K irradiation. Magnetic field perpendicular to c axis.

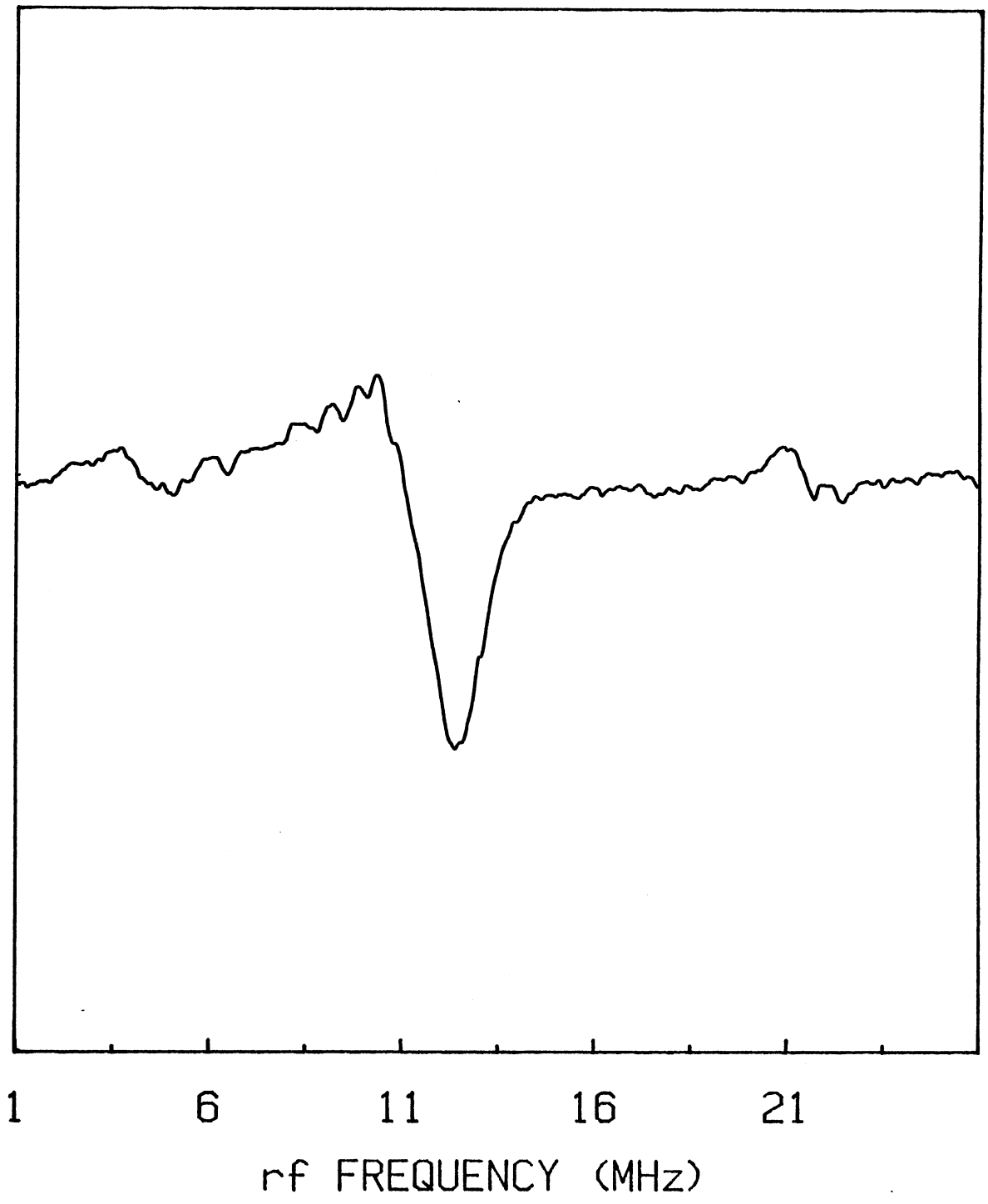

Figure 25. ENDOR spectrum of Ti^{3+} ions in $LiNbO_3$:Ti. Observed at 13 K after a high-temperature argon reduction. Magnetic field perpendicular to c axis.

CHAPTER IV

CONCLUSIONS

Our investigation of point defects in a series of lithium niobate crystals either undoped, codoped with magnesium and iron, or titanium doped has revealed considerable information about impurities and other defects produced by radiation and reduction treatments.

Room-temperature irradiation of undoped $LiNbO_3$ crystals converted approximately 50% of the trivalent iron ions (Fe^{3+}) into their reduced charge state (Fe^{2+} ions). It is not clear why further irradiation would not convert the remaining Fe^{3+} ions to the divalent charge state as is observed in the case of high temperature reduction treatments. These results suggests that other impurities or defects may be playing a role in forming or stabilizing the divalent iron ions after irradiation.

The defects produced either by irradiation or reduction in lithium niobate co-doped with iron and magnesium are basically of the same nature as those produced by similar treatments in lithium niobate doped only with magnesium above 4.5%. The observation, using a 35-GHz spectrometer, of a new ESR spectrum for Fe^{3+} ions suggested that the presence of Mg in lithium niobate significantly perturbs the

Fe^{3+} ions. Further investigation of this new spectrum and an analysis of its ESR spin-Hamiltonian is needed.

Our investigation of point defects in titanium-doped lithium niobate, after irradiation and reduction, reveals behavior very similar to the magnesium-doped lithium niobate for above threshold (4.5% Mg or above) levels. Reduction of $LiNbO_3$:Ti results in the formation of two strongly overlapping visible absorption bands. No significant change in these absorption bands upon exposure to visible/UV light at low temperature was observed. The significance of an approximate 20% increase in the intensity of the ESR spectrum of Ti^{3+} ions after a 77-K optical bleach is not clear. No F to F^+ conversion after optical bleaching at 77 K was observed. Although formation of an F^+ center after reduction is suggested, we were unsuccessful in attempts to observe an ESR spectrum of the F^+ center.

Observation of ENDOR spectra from Ti^{3+} ions in both reduced and irradiated samples of $LiNbO_3$:Ti has demonstrated the potential of this method to provide the detailed information needed to make a definitive defect model for the Ti^{3+} ions (i.e., actual site and surroundings). Although we did not perform a complete analysis of the complete ENDOR spin-Hamiltonian for the Ti^{3+} ions in $LiNbO_3$:Ti crystals because of its considerable complexities, the information obtained from such an effort would easily justify the difficulties.

REFERENCES

1. Zachariasen, W. H., Skr. Norske Vid.-Ada., Oslo, Mat. Naturv. 4 (1928).

2. Matthias, B. T., and J. P. Remeika, Phys. Rev. 76, 1886 (1949).

3. Ballman, A. A., J. Am. Ceram. Soc. 48, 112 (1965).

4. Fedulov, S. A., A. I. Shapiro, and P. B. Ladyzhenskii, Kristallografiya 10, 268 (1965).

5. Nassau, K., J. H. Levinstein, and G. M. Loiacono, J. Phys. Chem. Solids 27, 989 (1966).

6. Abrahams, S. C., J. M. Reddy, and J. L. Bernstein, J. Phys. Chem. Solids 27, 997 (1966).

7. Abraham, S. C., W. C. Hamilton, and J. M. Reddy, J. Phys. Chem. Solids 27, 1013 (1966).

8. Fay, H., W. J. Alford, and H. M. Dess, Appl. Phys. Lett. 12, 89 (1968).

9. Bergman, J. G., A. Ashkin, A. A. Ballman, J. M. Dziedzic, H. M. Levinstein, and R. G. Smith, Appl. Phys. Lett. 12, 92 (1968).

10. Lerner, P., C. Legras, and J. P. Dumas, J. Cryst. Growth 3, 231 (1968).

11. Carruthers, J. R., G. E. Peterson, M. Grasso, and P. M. Bridenbaugh, J. Appl. Phys. 42, 1846 (1971).

12. Peterson, G. E., and J. R. Carruthers, J. Solid State Chem. 1, 98 (1969).

13. Midwinter, J. E., Appl. Phys. Lett. 11, 128 (1967).

14. Scott, B. A., and G. Burns, J. Am. Ceram. Soc. 55, 225 (1972).

15. Abrahams, S. C., H. J. Levinstein, and J. M. Reddy, J. Phys. Chem. Solids 27, 1019 (1966).

16. Niizeki, N, T. Yamada, and H. Toyada, Jap. J. Appl. Phys. 6, 318 (1967).

17. Ashkin, A., G. D. Boyd, J. M. Dziedzic, R. G. Smith, A. A. Ballman, H. J. Levinstein, and K. Nassau, Appl. Phys. Lett. 9, 72 (1966).

18. Peterson, G. E., A. A. Ballman, P. V. Lenzo, and P. M. Bridenbaugh, Appl. Phys. Lett. 5, 62 (1964).

19. Chen, F. S., J. Appl. Phys. 40, 3389 (1969).

20. Lenzo, P. V., E. H. Turner, E. G. Spencer, and A. A. Ballman, Appl. Phys. Lett. 8, 81 (1966).

21. Turner, E. H., Appl. Phys. Lett. 8, 303 (1966).

22. Johnston, Jr., W. D., J. Appl. Phys. 41, 3279 (1971).

23. Glass, A. M., G. E. Peterson, and T. J. Negran, in Laser Induced Damage in Optic Materials, edited by A. J. Glass (Ntl. Bur. Std. Special Publication No. 372, U.S. GPO, Washington D.C., 1972), pp. 15-26.

24. Phillips, W., J. J. Amodei, and D. L. Staebler, RCA Rev. 33, 94 (1972).

25. Glass, A. M., Opt. Eng. 17, 470 (1978).

26. Bryan, D. A., R. Gerson, and H. E. Tomaschke, Appl. Phys. Lett. 44, 847 (1984).

27. Sweeney, K. L., L. E. Halliburton, D. A. Bryan, R. R. Rice, R. Gerson, and H. E. Tomaschke, J. Appl. Phys. 54, 1036 (1985).

28. Primak, W., T. T. Anderson, and S. L. Halverson, Nuclear Technology 10, 76 (1971).

29. Towner, J. B., Y. M. Kim, and H. S. Story, J. Chem. Phys. 56, 3676 (1972).

30. Herrington, J. B., B. Dischler and J. Schneider, Solid State Commun. 10, 509 (1972).

31. Mehran, F. and B. A. Scott, Solid State Commun. 11, 15 (1972).

32. Setser, G. G., Ph.D. Thesis, Rice University, 1975.

33. Rosa, J., K. Polak, and J. Kubatova, Phys. Stat. Sol. 111, K85 (1982).

34. Korradi, G., K. Polgar, A. A. Bugai, I. M. Zaritaskii, L. G. Rakitina, V. G. Grachev, and N. I. Deryugina, Sov. Phys. Solid State 28, 412 (1986).

35. Arsenev, P. A. and B. A. Baranov, Phys. Stat. Sol. 9(a), 673 (1972).

36. Sirota, N. N. and W. P. Yarunichev, Krist. und Tech. 12, 411 (1977).

37. Arizmendi, L., J. M. Cabrera, and F. Agullo-Lopez, Ferroelectrics 26, 823 (1980).

38. Bukharaev, A. A., S. A. Migachev, A. A. Monakhov, V. A. Golenishchev-Kutuzov, N. A. Shamukov, N. R. Yafaev, and N. B. Angert, Sov. Phys. Solid State 18, 350 (1976).

39. Ketchum, J. L., K. L. Sweeney, L. E. Halliburton, and A. F. Armington. Phys. Lett. A 94, 450 (1983).

40. Bollmann, W., and M. Gernand, Phys. Stat. Sol. (a) 9, 301 (1972).

41. Ohmori, Y., Y. Yasojima, and Y. Inuishi, Japn. J. Appl. Phys. 14, 1291 (1975).

42. Ho, F. D., Phys. Stat. Sol. (a) 66, 793 (1981).

43. Sweeney, K. L., and L. E. Halliburton, Appl. Phys. Lett. 43, 336 (1983).

44. Arizmendi, L., J. M. Cabrera, and F. Augullo-Lopez, J. Phys. C 17, 515 (1984).

45. Sweeney, K. L., L. E. Halliburton, D. A. Bryan, R. R. Rice, R. Gerson, and H. E. Tomaschke, Appl. Phys. Lett. 45, 805 (1984).

46. Schirmer, O. F., and D. Von der Linde, Appl. Phys. Lett. 33, 35 (1978).

47. Juppe, S., and O. F. Schirmer, Phys. Lett. A 117, 150 (1986).

VITA

Mohammad Reza Hantehzadeh

Candidate for the Degree of

Doctor of Philosophy

Thesis: INVESTIGATION OF POINT DEFECTS IN LITHIUM NIOBATE BY ELECTRON SPIN RESONANCE, ELECTRON NUCLEAR DOUBLE RESONANCE, AND OPTICAL ABSORPTION

Major Field: Physics

Biographical:

Personal Data: Born in Ahwaz, Iran, May 24, 1958, the son of Hossein H. and Mahin H. Married to Parvaneh Zarpoush on June 25, 1979.

Education: Graduated from Dr. Fatemi High School in Ahwaz, Iran, in May, 1976, received Bachelor of Science Degree in Electrical Engineering in May, 1981 from Oklahoma State University; received a Master of Science Degree in Physics from Oklahoma State University in May 1984; completed requirements for Doctor of Philosophy Degree in physics at Oklahoma State University in December, 1987.

Professional Experience: Teaching Assistant, Department of Physics, Oklahoma State University, August 1981 to May 1981; Lead Teaching Assistant, Oklahoma State University, June 1981 to July 1983, Radiation Safety Assistant, Oklahoma State University, August 1983 to February 1987; and Grduate Research Assistant, Oklahoma State University, March, 1987 to December, 1987.